מכון ויצמן למדע

WEIZMANN INSTITUTE OF SCIENCE

Thesis for the degree
Doctor of Philosophy

חבור לשם קבלת התואר
דוקטור לפילוסופיה

By
Nurit Avraham

מאת
נורית אברהם

מדידות מגנטיות מקומיות של מוליכי- על חמים ומגנטים מולקולריים

Local magnetization measurements of high-temperature superconductors and single molecule magnets

Advisor
Prof. Eli Zeldov

מנחה
פרופ' אלי זלדוב

November 2007

כסלו ה'תשס"ח

Submitted to the Scientific Council of the
Weizmann Institute of Science
Rehovot, Israel

מוגש למועצה המדעית של
מכון ויצמן למדע
רחובות, ישראל

This thesis is dedicated to my father, Matti Avraham, who passed away in August 2005. My father's curiosity and strong urge for understanding have inspired and motivated me through all these years. I miss his intriguing questions about my work and the look of wonder ignited in his eyes whenever I showed him the beauty in science.

עבודת דוקטורט זו מוקדשת לאבי, מתי אברהם, שהלך לעולמו באוגוסט 2005. סקרנותו הרבה של אבי והצורך שלו להבין דברים לעמקם הנחו אותי ונתנו לי השראה לאורך כל שנות עבודתי המדעית. אני מתגעגעת לשאלותיו מעוררות המחשבה ולאותו מבט של פליאה וקסם שניצת בעיניו בכל פעם שנחשף ליופיו של המדע.

ACKNOWLEDGEMENTS

There are many people I would like to thank for their help and support during all these years.

First and foremost I thank my advisor, Eli Zeldov, whose wisdom, knowledge, and commitment to high standards have shaped the way I think scientifically and professionally. His clear understanding of physics and probing questions have served to focus my thoughts and clarify the essential issues. Eli has given me a great deal of freedom to pursue the research directions I thought were important, and the support I needed to accomplish them.

I thank Myriam Sarachik who introduced me to the field of molecular magnets and served as my advisor during the year I spent in the City College of New York. Even though her time was limited, as a vice president of the APS, the warm hospitality I was received with made this year a pleasant one, and the valuable knowledge in physics she shared with me made it a rewarding one.

I also thank the members of my thesis committee, Amir Yacoby and Ady Stern, for the helpful and friendly way in which they followed my work. Ady Stern's interest in my work has led to a fruitful collaboration, not to mention endless discussions through which I broadened my theoretical horizons and came to share his immense enthusiasm for physics.

I thank Ernst Helmut Brandt, Grigorii Mikitik, Yadin Goldschmidt, Kees van der Beek, and Marcin Konczykowski for constructive collaboration and

major contribution to my work.

Special thanks to Yuri Myasoedov for putting his heart into preparing the samples and using his experience to solve many technical problems.

I also thank Tsuyoshi Tamegai for providing high quality samples, Michael Rapapport and Dimitry Linsky for solving many physical and technical problems, Hadas Shtrikman for the fine heterojunction growth, and my friends Sarah Goldberg, Tal Hazak, Haim Beidenkopf, Amit Finkler, Yehonathan Segev, and Beena Kalisky for always being ready for discussions and for making me laugh a lot.

Finally, I thank Gil Tayar, my husband, for helping in so many ways and for reminding me that time is always running.

CONTENTS

1. INTRODUCTION

The discovery of high-temperature superconductors in 1986 [1] renewed the interest in superconductors. These materials are Type II superconductors, in which external magnetic fields penetrate the material in the form of magnetic flux lines - vortices - forming a mixed state. The behavior of vortices, under various temperature and magnetic field conditions, is interesting both from the practical and scientific point of view.

From the practical point of view, the design and performance of superconductor based applications is often limited by the suppression of superconductivity at intense magnetic fields. In the mixed state, resistance to current flow can occur since the vortices tend to move in the presence of applied currents due to the Lorentz force. This motion of vortices perpendicular to the current produces energy dissipation and an effective resistance in the superconductor appears. Knowing how the vortices move and arrange themselves under various temperature and magnetic field conditions will be critical in controlling the phenomena and in maintaining a dissipationless current.

From the scientific point of view, the vortex matter system is very attractive as it provides a remarkable example of a condensed matter state with tunable parameters [2], enabling the study of general phase transition behavior. Experimentally, all the relevant parameters can be varied over wide ranges - the vortex density can be changed by varying the external magnetic field, thermal fluctuation can be changed by varying the tempera-

ture, quenched disorder can be modified through controlled irradiation, and the coupling energy between the CuO_2 layers can be altered through the choice of material. The vortex matter in high-temperature superconductors exhibits a very complicated phase diagram consisting of a variety of liquid and solid phases and transitions among them - some of which are still not well understood.

In this research work, we use magneto-optic techniques to investigate the phase diagram of $Bi_2Sr_2CaCu_2O_8$ crystals in the presence of different types of pinning centers. We focus on the effect of columnar defects and tilted columnar defects on the dynamic and thermodynamic properties of the vortex matter. In order to overcome the difficulties arising from the non-equilibrium conditions, we implement the "shaking" technique, using an in-plane ac magnetic field. This technique was found to equilibrate the vortex lattice in $Bi_2Sr_2CaCu_2O_8$ superconductors at low temperatures, enabling the observation of equilibrium vortex properties.

Another form of magnetic materials investigated in this work is single molecule magnets. These organic materials provide an ensemble of nearly identical molecules with negligible inter molecule interactions and small environmental interactions. As a consequence, *macroscopic* samples of these organic materials exhibit dramatic quantum mechanical phenomena like tunneling of magnetization [3] and Berry phase oscillations [4]. In this work we use Hall sensor arrays to study the effect of dipolar interactions on the spatial distribution of the magnetization inside single molecule magnets.

This work is divided as follows:

- The scientific background, briefly describing the basic phenomena and theory of superconductivity and single molecule magnets relevant to this work, is described in chapter 2 and 3.

- The methodology of, and the motivation for, the specific experimental techniques are given in chapter 4.
- Chapter 5 and 6 provide the description of the experimental setups for the magneto-optical measurements and for the Hall sensors measurements.
- Presentation and discussion of experimental results are provided in chapter 7.
- Chapter 8 summaries the results.
- A list of publication is given in chapter 9.

2. SUPERCONDUCTIVITY

2.1 Basic characteristics

The electrical resistance of many metals and alloys vanishes abruptly when they are cooled below a certain temperature T_c, which is a characteristic of the material. This phenomenon of superconductivity was discovered by Kamerlingh Onnes [5] in Leiden in 1911, three years after he first liquefied Helium. At the critical temperature T_c, the material undergoes a phase transition from a state of normal electrical resistivity to a superconducting state. It was immediately recognized that this phenomenon is of vast potential importance in technology because it means that current can flow through a superconducting material without any losses. Current induced in a superconducting ring, for example, has been demonstrated to persist for several years without any diminution - where no battery of any kind was present. Thus, perfect conductivity is the first important property of superconductivity. Another important property of superconductivity is perfect diamagnetism. In 1933 two German physicists, Meissner and Ochenfeld [6], found that superconductors expel magnetic fields. If a superconductor in its normal state is put in a magnetic field, and the temperature is lowered below the critical temperature, the magnetic field is expelled. The property of perfect diamagnetism is not a direct consequence of perfect conductivity. Maxwell equations predict that the magnetic field inside a perfect conductor

is time independent, implying that if there is magnetic flux inside a perfect conductor above T_c it will remain there when the sample is cooled below its T_c. The expulsion of magnetic flux out of a superconductor is known as the Meissner effect, and it takes place through the appearance of surface currents in a thin layer of the material. These currents create a magnetic field that cancels the external field inside the superconductor. Another important property, common to most superconductors, is the existence of an energy gap in the density of states. The energy gap [7] is of the order of $k_B T_c$ and it is centered around the Fermi energy. A direct consequence of the gap is the peculiar behavior of the heat capacity. As the temperature is decreased a sudden jump to a value above that of the normal metal is observed near T_c, followed by a low temperature behavior of the form $\exp(-\Delta/k_B T)$.

2.2 Theory of superconductivity

2.2.1 London theory

A phenomenological theory [8] which explains some of the properties of superconductors was proposed in 1935 by the brothers Fritz and Heinz London. The first equation in their theory is based on Ohm's law and accounts for perfect conductivity by postulating an infinite scattering time for the charge carriers. It relates the local electric field $\mathbf{E}$ to the supercurrent density $\mathbf{j}$ by

$$\mathbf{E} = \frac{\partial}{\partial t}(\Lambda \mathbf{j}) \tag{2.1}$$

where $\Lambda = \mu_0 \lambda_L^2 = m/n_s e^2$. Here m, n_s and e are the mass, density and the charge of the superconducting electrons and λ_L is the London penetration depth. The second London equation postulates that the supercurrent density $\mathbf{j}$ is proportional to the vector potential $\mathbf{A}$,

$$\mathbf{j} = \frac{1}{\mu_0 \lambda_L^2} \mathbf{A}. \tag{2.2}$$

Taking into account that $\mathbf{B} = \nabla \times \mathbf{A}$, Eq.(2.2) can be written in the form

$$\nabla \times \mathbf{j} = \frac{1}{\mu_0 \lambda_L^2} \mathbf{B}. \tag{2.3}$$

Combining Eq. (2.3) With Maxwell's equation $\nabla \times \mathbf{B} = \mu_0 \mathbf{j}$ leads to

$$\nabla^2 \mathbf{B} = \frac{\mathbf{B}}{\lambda_L^2}. \tag{2.4}$$

The only solution for this equation is an exponential decay of $\mathbf{B}$ with λ_L as the length over which the field penetrates inside the superconductor. In this way, Eq. (2.4) describes the Meissner state.

2.2.2 The Ginzburg-Landau theory

A new phenomenological theory [9, 10] that contains London theory and explains rather well the behavior of superconductors in an applied field, was proposed in 1950 by V. L. Ginzburg and L. D. Landau. Although their theory is based on the free energy expansion near T_c, its main results remain valid in the entire range of temperatures.

The Ginzburg-Landau (GL) theory is based on three fundamental assumptions:

1. There exist an order parameter Ψ, which goes to zero at the transition.
2. The free energy may be expanded in powers of Ψ.
3. The coefficients are regular functions of T.

The expansion of the GL free energy density, when Ψ is a complex nonlocal variable, is given by

$$f = f_n + \alpha|\Psi|^2 + \frac{\beta}{2}|\Psi|^4 + \frac{1}{4m}|(\frac{\hbar}{i}\nabla - \frac{2e}{c}\mathbf{A})\Psi|^2 + \frac{\mathbf{H}^2}{8\pi} \tag{2.5}$$

Here f_n is the free energy density of the normal state at zero magnetic field while α and β are parameters depending on the temperature and the material. Minimizing the free energy obtained by integrating Eq. (2.5) over the sample volume, leads to the GL equations

$$\alpha|\Psi| + \beta|\Psi|^2\Psi + \frac{1}{4m}(\frac{\hbar}{i}\nabla - \frac{2e}{c}\mathbf{A})^2\Psi = 0 \tag{2.6}$$

$$\mathbf{j} = \frac{e\hbar}{2mi}(\Psi^*\nabla\Psi - \Psi\nabla\Psi^*) - \frac{2e^2}{mc}\Psi^*\Psi\mathbf{A} \tag{2.7}$$

Equation (2.6) gives the variation of Ψ once we know the vector potential $\mathbf{A}$, while equation (2.7) gives the current distribution. The two GL equations have two special solutions:

$\Psi = 0$ where $\mathbf{A}$ is determined only by $\mathbf{H} = \nabla \times \mathbf{A}$. This solution describes the normal state.

$\Psi = \Psi_0 = (-\alpha/\beta)^{1/2}$ and $\mathbf{A} = 0$, this solution describes the ordinary superconductor state, with perfect Meissner state.

There are two characteristic lengths, which can be deduced from the equations in the limit of weak magnetic fields. From equation (2.6) we can obtain the coherence length $\xi(T) = -\hbar^2/2m\alpha$, which characterizes the distance over which $\Psi(r)$ decreases to zero. From Eq. (2.7) we can obtain the penetration depth $\lambda(T) = (mc^2/16\pi e^2\Psi_0^2)^{1/2}$, which characterizes the distance of penetration of the magnetic field into a superconducting region. The ratio of these two characteristic lengths defines the GL parameter $\kappa = \lambda/\xi$, which determines the magnetic behavior of the material, and differentiates between different types of superconductors.

2.2.3 BCS theory

The phenomenological London and Ginzburg-Landau theories explain many characteristic features of superconductivity. However, they do not provide any information about its origin or nature. In 1957, Bardeen, Cooper, and Schrieffer developed a microscopic theory of superconductivity, known as the BCS theory [11, 12]. In 1956 L. N. Cooper had studied [13] the interaction of a pair of electrons near the Fermi surface. He considered the problem of two electrons with an attractive interaction via phonos and demonstrated that in the presence of a Fermi sphere of additional electrons, the ground state of the system would be a bound state. As long as there is a net attractive interaction, no matter how weak, the formation of a bound pair would be energetically favorable for the system. The physical idea lies in the origin of this attractive interaction is the following - when the first electron travels through the lattice it attracts the positive ions of the lattice and creates a polarization in the system. The second electron is in turn attracted by the positive region created by the first electron. Effectively, two electrons are attracted to each other, by means of lattice oscillations. The attraction will take place if the oscillations of the electron density are slow enough so that the lattice can follow them. Bardeen, Cooper and Schrieffer took an essential step further and constructed a ground state in which all electrons are bound into pairs. This ground state is separated from the excited states by an energy gap. As long as the thermal energy is less than the gap, the electrons will not have enough energy to collide with the lattice and the resistivity will be zero. In fact, collisions occur, but they just lead to an exchange of partners, so the correlated motion that creates zero resistivity is conserved. The size of the pairs is given by the coherence length ξ, which can be up to a few μm in some conventional superconductors. This length is much larger

than the spacing between electrons, so the pairs strongly overlap.

2.3 The mixed state in Type II superconductors

Superconductors can be divided into two different types, depending on the value of the GL parameter κ. The classical pure superconductors like lead or tin, with $\lambda < \xi$ and therefore $\kappa < 1$, are known as Type I superconductors. In this kind of materials, the magnetic field is totally excluded from the material up to a critical field H_c. Above H_c the system undergoes a first-order transition into the normal state and superconductivity is destroyed. In type II superconductors, the perfect superconducting state with a total

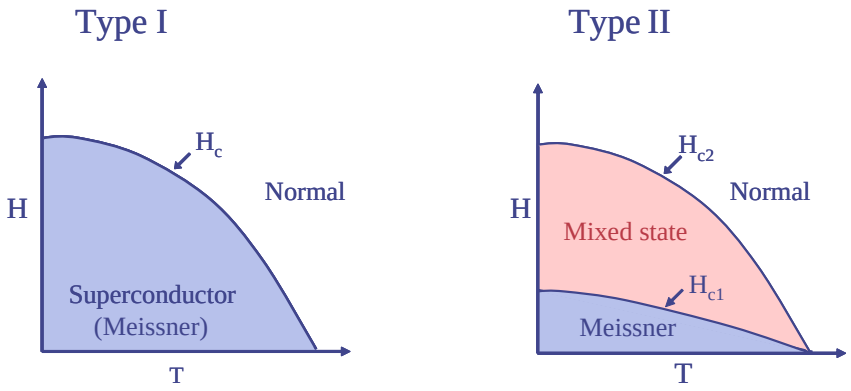

Fig. 2.1: H-T phase diagrams of Type I and Type II superconductors.

expulsion of the magnetic field exists up to a lower critical field H_{c1}. However, instead of a discontinuous transition to the normal state, at H_{c1} the magnetic field starts to penetrate into the material in the form of quantized flux lines, or vortices, and form the so called mixed state. A schematic phase diagram of both types is shown in Fig. 2.1.

The mixed state of Type II superconductors was derived by Abrikosov in 1957 [14, 15]. Based on the GL theory, he predicted that the magnetic field in

Type II superconductors would penetrate the sample as quantum flux lines that form a hexagonal array known as the Abrikosov vortex lattice. This vortex lattice has been observed using different techniques such as magnetic decoration [16], neutron scattering [17, 18], electron microscopy [19], electron holography [20], and Hall probe microscopy [21].

The structure of an individual vortex (Fig. 2.2) depends on the coherence length and penetration depth. The vortex has a normal core whose radius is the coherence length. The normal core is surrounded by supercurrents that produce magnetic field. Thus, in the center of the normal core, the magnetic field has its highest value, and it decays exponentially with a characteristic length λ. The total magnetic flux each vortex contains is exactly one quantum of magnetic flux $\Phi_0 = hc/2e = 2.07 \times 10^{-7}$ Gcm^2. The vortices repel one another and hence spread out over the entire sample volume and form the Abrikosov lattice.

The origin of the mixed state lies in the surface energy of the interface between the superconducting and normal phases. For the boundary to be in equilibrium, the Gibbs free energy on each side must be the same. Consider the change in energy in going from the superconducting to the normal side of the boundary. The change is not abrupt since Ψ decreases to zero over a distance ξ. Hence, we pay an energetic cost of $\sim \frac{H_c^2}{8\pi}\xi$ per unit area, because of loss of condensation energy on a scale ξ. On the other hand the magnetization energy is reduced by $\sim \frac{H_c^2}{8\pi}\lambda$ per unit area, since the magnetic field penetrates a distance λ into the superconducting phase. Thus, the surface energy per unit area is $E_{surf} \sim \frac{H_c^2}{8\pi}(\xi - \lambda)$. This means that for $\kappa \ll 1$ we have a positive surface energy with Type I behavior, whereas for $\kappa \gg 1$ the surface energy is negative resulting in type II behavior. A precise calculation within the framework of the GL theory [22], shows that the surface energy changes sign

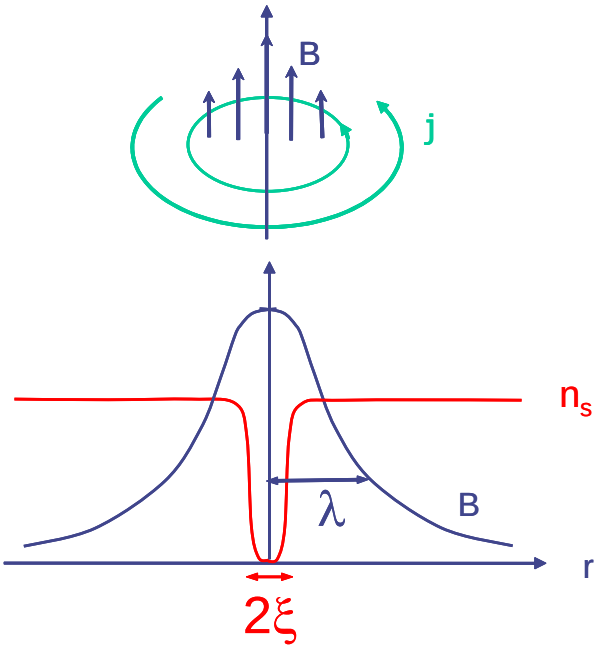

Fig. 2.2: Structure of a vortex line in a Type II superconductor. The vortex line is surrounded by a current loop. The magnetic field B is at its maximum near the center of the line. Going outwards, B decreases to zero with characteristic length λ. The density of superconducting electrons, n_s, is reduced only in a small "core region" of radius ξ.

at $\kappa = 1/\sqrt{2}$. The appearance of a normal region in type II superconductors lowers the Gibbs free energy. It is, therefore, energetically favorable for the material to split up into a large number of small normal filaments to produce a maximum boundary area.

The behavior of the magnetic vortices constituting the mixed state is intimately related to the most important practical defining characteristic of the superconducting state - its ability to carry an electrical current without loss. The central idea is that the moving vortices dissipate energy. When an applied current flows through a superconductor in its mixed state, there is a Lorentz force between the current and the magnetic flux lines. The force on

a single line is given by $\mathbf{F} = \mathbf{J} \times \mathbf{\Phi_0}$, where $\mathbf{J}$ is the transport current density, and $\mathbf{\Phi_0}$ is a vector of magnitude $hc/2e$ directed along the flux line. Because of this force, flux lines tend to move transverse to the current. If the vortices move with velocity $\mathbf{V}$, they induce an electric field $\mathbf{E} = \mathbf{B} \times \mathbf{V}/c$, which is parallel to $\mathbf{J}$. This acts as a resistive voltage, and power is dissipated. This means that an ideal superconductor in its mixed state does not display perfect conductivity. Thus, in order to achieve zero resistivity in a Type II superconductor in its mixed state, one should prevent all vortices from moving. This can be obtained by the introduction of artificial pinning centers e.g. through irradiation.

2.4 Vortex matter in High-T_c superconductors

In 1986, Bednorz and Müller [1], from the IBM Zurich Research Center, discovered a new class of Type II superconductors. These materials, a family of copper oxide ceramics, were found in some cases to superconduct at a temperature that exceeded 140 Kelvin. This discovery was surprising and exciting not only because of the large increase in T_c, but also because these materials can easily be cooled by liquid Nitrogen instead of liquid Helium - which implies economical advantages. High-temperature superconductors (HTSC) are not well described by BCS theory. The mechanism of superconductivity and the symmetry of the order parameter in HTSC is, in fact, one of the most controversial issues in superconductivity.

The HTSC are extreme Type II materials - they have short coherence lengths and long penetrations depths, which results in large values of the GL parameter κ. A direct consequence of a large κ is that the mixed state extends over a large part of the H-T phase diagram. This is clear if we look at the expressions for the lower and upper critical fields which confine the

mixed state. Magnetic flux penetrates into the superconductor when the Gibbs free energy of the system with one vortex becomes smaller than the Gibbs energy in the pure Meissner state. This occurs at fields just above the lower critical field H_{c1},

$$H_{c1} = \frac{\Phi_0}{4\pi\lambda^2} ln \frac{\lambda}{\xi}. \tag{2.8}$$

A long penetration depth λ leads to a low value of H_{c1} and therefore the Meissner state in high-T_c materials is confined to small fields. At the upper critical field H_{c2} the vortices are dense and their cores begin to overlap. From GL theory H_{c2} is found to be

$$H_{c2} = \frac{\Phi_0}{2\pi\xi^2}. \tag{2.9}$$

Short coherence length ξ, therefore, leads to H_{c2} which is much larger than in conventional superconductors. The vortex state occupies, thus, a large part of the phase diagram of high-T_c materials.

Soon after the discovery of the copper oxide high-temperature superconductors, it was shown that the resistivity in the temperature and magnetic field regime where the Abrikosov lattice was expected to form, behaves in a qualitatively different fashion from that found in previously studied Type II superconductors [23]. The reason for the difference is that strong thermal fluctuations cause the vortex lattice to melt into a vortex liquid well below the upper critical field H_{c2}. Strong thermal fluctuations in HTSC results from the combination of high operating temperatures, short superconducting coherence length, long penetration depth, and high anisotropy [24]. These materials are built of superconducting CuO_2 planes coupled by Josephson tunneling between adjacent layers and separated by blocking layers of normal metallic or insulating materials that act as potential barriers against

the tunneling of super-electrons between planes. If the coupling between layers is weak compared to thermal energies, the vortex lines behave more like strings of points or "pancake" vortices in each superconducting layer, with only rather weak correlation between vortices in different layers. The weak coupling between the layers, therefore, leads to highly flexible vortices. In the absence of thermal fluctuations and of pinning induced disorder, the vortex lattice is present at all fields below H_{c2}. However, in the presence of strong thermal fluctuations the vortex lines in the lattice vibrate with larger amplitudes as the temperature rises. At sufficiently high temperatures, the lines vibrate enough to cause melting of the vortex lattice. The melting transition occurs when the energy of thermal fluctuations becomes equal to the elastic energy barriers keeping vortices near their equilibrium positions in the lattice [25]. Theoretically, it is expected that this transition would occur by way of a first-order transition in clean systems [26], with a gradual transition in systems with quenched disorder [2]. Extensive experimental studies, including transport [27, 28], magnetization [29, 30], AC susceptibility [31], and calorimetric methods [32] confirmed the existence of such a first-order transition in relatively clean $YBa_2Cu_3O_7$ and $Bi_2Sr_2CaCu_2O_8$ crystals.

Figure 2.3 shows a schematic phase diagram of high-temperature superconductors. In perfectly clean and ideal materials, the vortex liquid freezes into a regular lattice on decreasing the temperature. In the presence of chemical and structural imperfections, however, it is energetically favorable for the vortices to reside on material imperfections. This pinning disrupts the regular lattice pattern and turns the vortex lattice phase into a vortex glass phase.

This rich equilibrium behavior of vortex matter in HTSC arises from the competition of three energies: Vortex interaction energy, keeping vortices

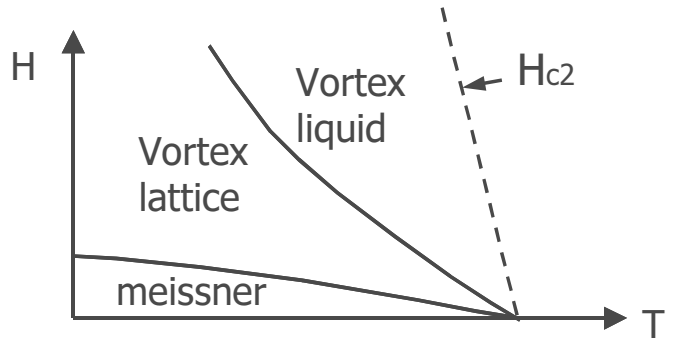

Fig. 2.3: Schematic phase diagram of HTSC.

near their equilibrium positions in the lattice; thermal energy favoring the vortex liquid state; and pinning energy, which describes the interaction of vortices with disorder-induced potential and favors the glassy solid state. In addition, there is the coupling energy which determines the flexibility of the flux line. HTSC have the advantage that all these energies can be of the same order of magnitude, resulting in a variety of liquid and solid phases. The vortex matter, thus, provides a remarkable example of condensed state for exploring general phase transition phenomena [2].

Further investigations [33, 34, 35, 36, 37], in the presence of disorder, reveal even more complicated phase diagrams. The experimental $H-T$ phase diagram of the vortex matter in $Bi_2Sr_2CaCu_2O_8$ (BSCCO) crystals is shown schematically in Fig. 2.4. The phase diagram is believed to consist of four distinct phases separated by a first-order melting transition $H_m(T)$ [29, 36], which is intersected by a second-order glass transition $H_g(T)$. At low fields, elastic interaction governs the structure of the vortex matter, forming the Bragg glass (BrG) phase in which a well defined lattice structure is preserved and long range order is only weakly perturbed. At high temperatures, thermal fluctuations melt the vortex-lattice into a vortex liquid phase. At

low temperatures the influence of quenched disorder effectively increases with increasing magnetic field, and at some characteristic field the pinning energy dominates the elastic-energy, leading to the transition from the BrG to the highly-disordered vortex glass phase. This amorphous glass phase is characterized by high concentration of dislocations and dynamics that is governed by plastic deformations. Thus, the quasi-ordered glassy phase is destroyed by a unified first-order transition, $H_m(T)$, that gradually changes its character from a thermal melting, at high temperatures, to a disorder-induced transition, at low temperatures. At low temperatures, this transition was found to display an unusual inverse melting behavior [36], where a disordered vortex glass phase transforms into an ordered lattice with increasing temperature. The $H_g(T)$ line, separating the amorphous glass and the vortex liquid phases, above the melting line, was observed experimentally using both dynamic and thermodynamic measurements [37, 38]. This second-order line marks the temperature above which the pinning centers stop being effective and vortices become mobile. This line was found to extend down into the BrG phase, suggesting a division of the BrG into two phases - the BrG and a thermally depinned vortex lattice phase.

Introduction of disorder in terms of point defects or columnar pins affects both the properties of the solid and liquid phases and also shifts the location of the melting transition in the $H - T$ plane. It has been shown that weak point disorder, produced by electron irradiation, shifts the melting transition to lower temperatures while preserving its first-order nature [39, 40, 41]. In the presence of high concentration of columnar defects (CDs), the vortex matter is believed to form a Bose glass phase [2] which is a strongly pinned, homogeneously disordered and anisotropic state. Significant progress has been achieved recently in understanding also the phase diagram of vortex

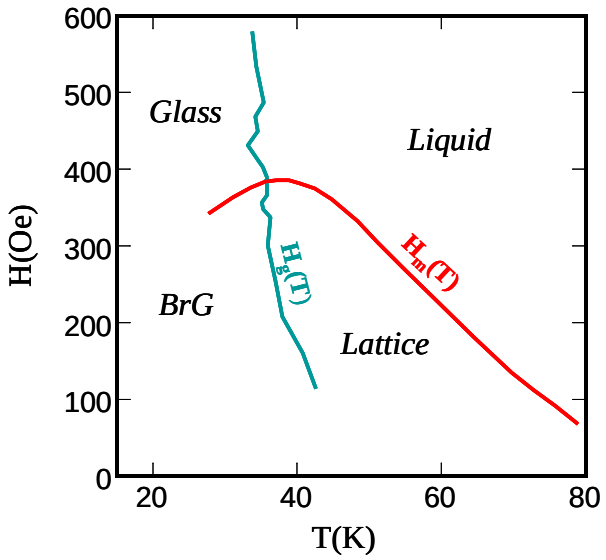

Fig. 2.4: The thermodynamic phase diagram of BSCCO. Four distinct phases, separated by a first-order melting line $H_m(T)$, which is intersected by the second-order glass line $H_g(T)$.

matter in the presence of low concentration of CDs, where vortices outnumber CDs. The picture that arises from experiments [42, 43, 44] and theoretical works [45, 46, 47, 48, 49, 50] is that of a "porous" vortex matter [42] which consists of two subsystems of vortices that are very different in nature; vortices that are localized on pinning centers and the interstitial vortices that reside between them. Fig. 2.5 shows a thermodynamic phase diagram in BSCCO in the presence of a low concentration of CDs.

At low temperatures, a *"porous" vortex solid* phase is created. In this phase a rigid matrix of vortices, strongly pinned on a network of random CDs, is formed, while the interstitial vortices create relatively ordered nanocrystals within the pores of the matrix. When increasing the temperature, the interstitial vortices melt, at $H_m^{cd}(T)$ while the rigid matrix remains unaltered, forming a *nanoliquid* phase in which nanodroplets of liquid are weakly

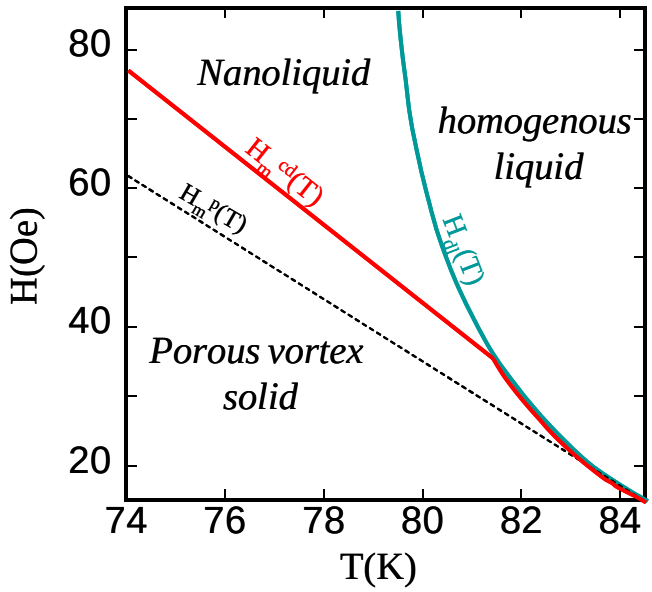

Fig. 2.5: The high temperature region of the thermodynamic phase diagram, in BSCCO, in the presence of a low concentration of CDs.

confined within the pores of the rigid matrix. An important property of this phase is that it has high correlation along the CDs but zero transverse critical current. When further increasing the temperature, the rigid matrix delocalizes at the delocalization transition, $H_{dl}(T)$, and the liquid becomes *homogeneous*.

In this work we study the dynamic and thermodynamic properties of the porous vortex matter in the presence of tilted CDs. We address the dependence of the melting and delocalization transitions on the angle between the CDs and the direction of the magnetic field. In further measurements we use the shaking technique to equilibrate the vortex matter and to investigate the equilibrium behavior of the vortex matter near the lower critical field in the presence of CDs.

3. SINGLE MOLECULE MAGNETS

A single molecule magnet is a tiny ferromagnet - at low enough temperatures the molecule can be magnetized by the application of an external magnetic field and it maintains its magnetization even when the external field is removed. Increasing the temperature above a critical temperature destroys the remanent magnetization and the molecule behaves like a paramagnet. The properties that are responsible for this magnetic behavior are the molecule's large spin and its easy axis anisotropy, which results in a barrier between up and down spin orientations. This gives rise to slow relaxation and to hysteretic behavior whose origin is the anisotropy of the individual molecule and not the motion of domain walls, as in conventional ferromagnets. For example, Mn_{12}-acetate - the most studied of the molecular magnets - exhibits hysteresis at temperatures below 3 K [51, 52, 53, 3] and, at the lowest temperatures, the time scale for a spin to flip can be many years [54].

The magnetic properties can be understood by the examination of the spin Hamiltonian. To the first approximation, the spin Hamiltonian of a single molecule magnet can be described by

$$H = -DS_z^2 - g_z\mu_B B_z S_z - AS_z^4 + V_T$$

where, the first term represents the magnetic anisotropy when the easy axis is taken along the z direction. This term describes the potential barrier the spin has to overcome in order to reverse its magnetization. The third term represents the next higher order term in longitudinal anisotropy. The

second term is the Zeeman coupling to a magnetic field B applied along the anisotropy axis of the molecule. The last term is the symmetry breaking term. V_T contains terms that do not commute with S_z and therefore produce tunneling.

One of the most investigated molecules is Mn_{12}. Its chemical formula is $[Mn_{12}O_{12}(CH_3COO)_{16}(H_2O)_4] \cdot 2CH_3COOH \cdot 4H_2O$. It consists of a magnetic core surrounded by a non-magnetic host. As shown in Fig. 3.1 the mag-

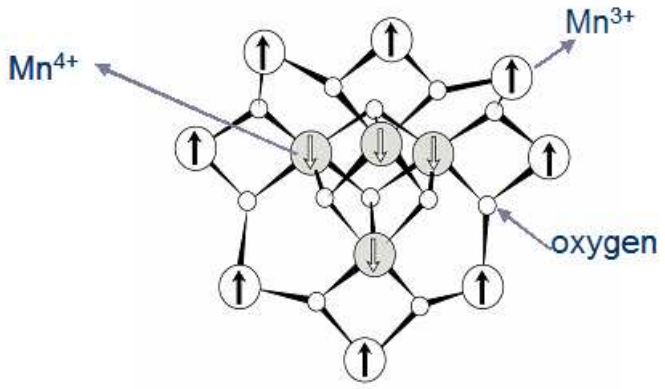

Fig. 3.1: The magnetic core of Mn_{12}-acetate. The four inner Mn^{4+} ions couple anti-ferromagnetically via superexchange bridges to the eight outer Mn^{3+} ions.

netic core consists of four Mn^{4+} ions symmetrically arranged on the corners of a cuban, surrounded by eight Mn^{3+} ions situated on an outer noncoplanar ring. The two rings are antiparallel, yielding a ferromagnetic ground state with a total spin $S = (8 \times 2) - (4 \times 3/2) = 10$. The magnetic anisotropy results from the spin-orbit coupling of the electrons and the uniaxial symmetry of the molecule. The second order contribution to the anisotropy DS_z^2 can be calculated using second order perturbation theory with spin orbit coupling [55].

This system can be modeled by a symmetric double well potential with

a set of energy levels corresponding to the $(2S+1) = 21$ energy levels of the quantum number S_z. The potential energy in the easy-axis plane is shown schematically in Fig. 3.2a. The vertical axis represents the energy of the eigenvalues and the horizontal axis represents the angle the spin operator makes when projected along the z-axis. In the absence of a magnetic field (Fig. 3.2a), the magnetization has two equivalent energy minima, corresponding to being aligned parallel or antiparallel to the z axis. In order to switch from one minimum to another, the system has to overcome a barrier of energy $U = DS^2$. Applying a magnetic field along the z direction tilts the potential, creating a stable and a metastable well (Fig. 3.2b). The molecule will then occupy the lower side of the well.

One of the most interesting phenomena that was found in Mn_{12} is the resonant tunneling of the magnetization. At zero magnetic field, states on opposite sides of the barrier are degenerate. When the field increases, the degeneracy is lifted, but at particular values of the applied field, all the energy levels in the unstable well will once again become degenerate with energy levels in the stable well. It was found [3] that whenever levels on opposite sides of the barrier are brought into such resonances, the relaxation of the magnetization is enhanced. This phenomenon manifests itself by steep steps in the hysteretic magnetization loop of the Mn_{12} crystals.

When crystalized, the Mn_{12} molecules form a tetragonal lattice in which the molecules are all aligned with the easy axis parallel to the c axis of the crystal. The nonmagnetic host of the molecule keeps molecules in different cells far apart so that the exchange interaction between the molecules is negligible. Therefore the magnetic properties of the crystals approximately represent the magnetic properties of the individual molecule. Nevertheless there exist some weak interactions, mainly dipolar interactions between the

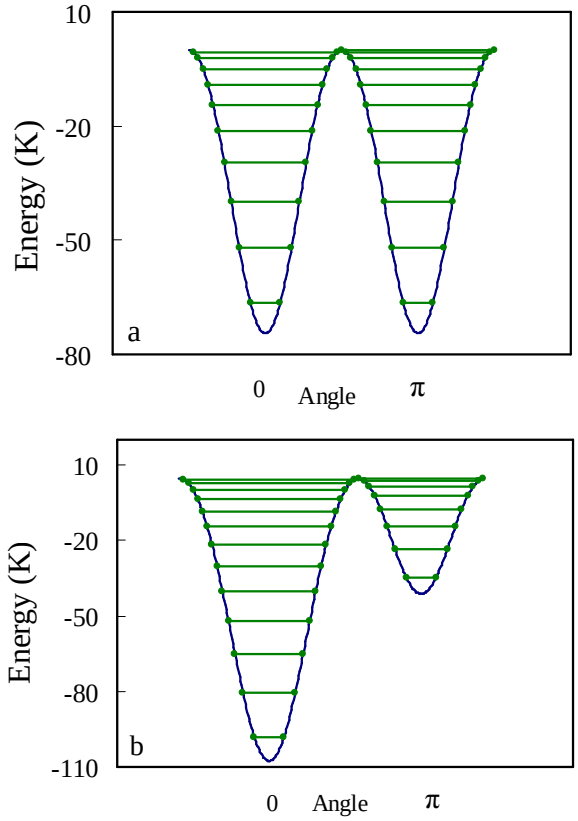

Fig. 3.2: Double well potential for $H = -DS_z^2 - g_z\mu_B B_z S_z - AS_z^4 + V_T$, with $S = 10$, for $H_z = 0$ (a) and for $H_z \neq 0$ (b).

molecules. In this work we study the effect of these interactions on the magnetization of the crystal.

4. METHODOLOGY

4.1 Magneto-optical measurements

A common way to image the distribution of the magnetic field at the surface of superconductors is to bring a magneto-optically (MO) active film into intimate contact with the sample and to examine it under linearly polarized light. The contrast achieved between regions of different magnetic field is a consequence of the Faraday rotation of the polarization of the incident light. Farady effect is the ability of certain materials to rotate the polarization plane of the transmitted light in the presence of magnetic field. The rotation results from the change in the carrier motion induced by the applied magnetic field. For a linearly polarized light propagating in the medium parallel to the direction of the magnetic field, the angle of rotation is given by the empirical law $\alpha = VlB$, where V is the Verdet coefficient, B is the magnetic field value, and l is the thickness of the medium.

The MO technique was established in our Lab a few years ago and is described in detail in [56]. Following is a short summary describing the system and the various MO techniques we used in the present study.

In our MO measurements the superconducting sample is brought into intimate contact with a magneto optically active film and examined under linearly polarized light. Fig. 4.1 shows a schematic view of the MO system. The MO indicator, which is an iron-garnet film with an in-plane magnetiza-

tion, is placed on top of a superconductor sample. A linearly polarized light is reflected from the bottom mirror of the indicator and undergoes a Faraday rotation within the indicator. The angle of rotation of the polarization is proportional to the local magnetic field. After passing through a perpendicularly polarized analyzer, a real time optical image is obtained, in which the local brightness is directly related to the intensity of the local magnetic field. The resulting image is captured by a CCD camera and is transferred to a computer. In conventional MO measurement, a sequence of images is taken while the applied magnetic field is swept.

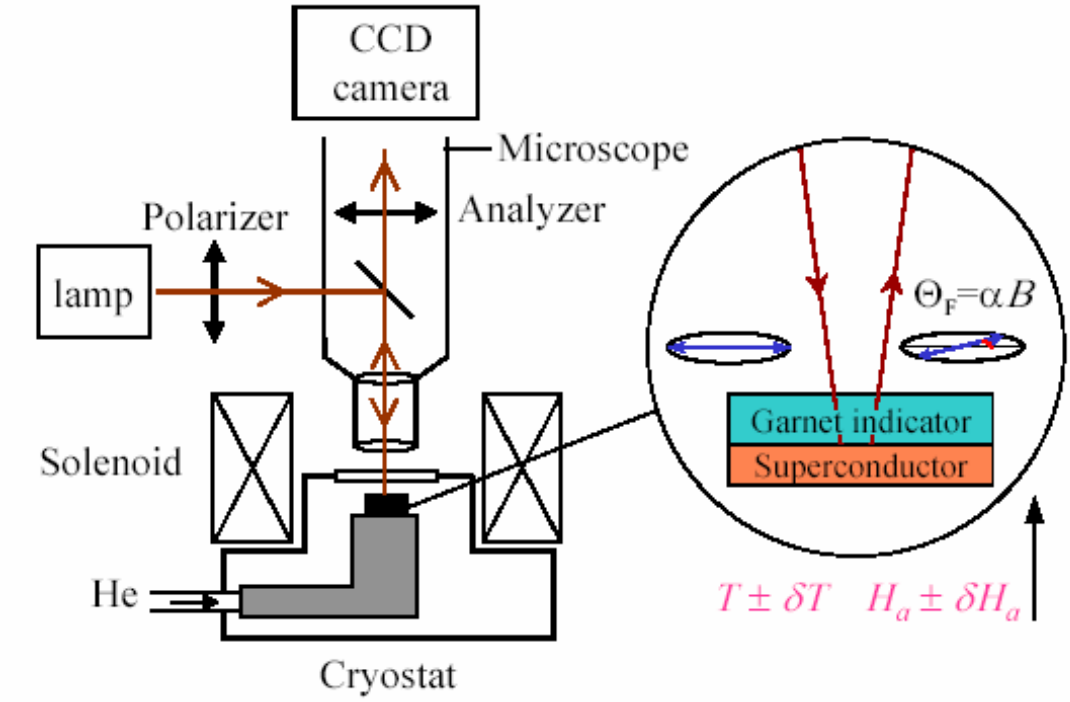

Fig. 4.1: Schematic view of the magneto-optical system.

In order to study the melting transitions we have used the differential magneto-optical (DMO) method [56, 57]. This method provides high field sensitivity which enables the detection of local field variations of the order of

tenth of a Gauss on a background field of several hundred Gauss. In DMO measurements, we first fix the applied field and the temperature, and acquire a set of images and average them. Then the magnetic field or temperature is increased by a very small amount and another set of images is acquired and averaged. We than subtract the first averaged image from the second one and obtain the resulting differential image. This process is repeated and averaged typically 100 times in order to improve the signal to noise ratio. By recording the differential images in a sequence of fields or temperatures a movie of the melting process is obtained.

In order to study the transport current flow in HTSC we used the DMO self-field method. This method enables us to study the transport current flow in HTSC. The method provides a two-dimensional visualization of the flow of small transport currents. In this method the difference between the MO images, taken with and without the current flowing in the crystal, provides an image of the self-induced magnetic field generated by the current. The two-dimensional current flow can be derived from the self-field by inversion of the Biot-Savart law. In fact, the image of the self-field is obtained from difference between the MO images taken with positive and negative currents flowing in the crystal. This procedure prevents possible artifacts, which may result from sample heating by the current.

In the present study we improved the system by adding the shaking method to it. This extended the H-T range in which MO measurements can be done in equilibrium conditions.

4.2 The shaking method

Experimental investigation of the equilibrium properties of Type II superconductors can be performed only in the reversible region of the H-T phase

diagram. Unfortunately, in most superconductors the reversible region is very narrow owing to the onset of irreversibility by pinning effects at lower temperatures. In the shaking method we apply an additional oscillating magnetic field perpendicular to the main dc field. This in-plane ac field reduces the irreversible magnetization [36, 58] and therefore extends the observable domain in the H-T plane in which experimental investigation of equilibrium properties can be made. In BSCCO crystals this method can fully suppress the magnetic hysteresis down to about 28K. The Abrikosov vortices in BSCCO can be regarded as a stack of Josephson coupled pancakes in the individual layers of the material. The in-plane ac field penetrates through the sample in the form of Josephson vortices between the layers [59]. The interaction between the Josephson vortices supercurrent and the pancake vortices induces a weak local agitation of pancake vortices [59] which assists thermal activation in relaxing the irreversible magnetization and in approaching thermal equilibrium. Theoretical works for non-layered materials [60] have shown that a weak ac magnetic field in the plane of a thin superconducting platelet allows the vortices to drift. This vortex motion generates a dc voltage in the superconductor that causes the critical currents and irreversible magnetic moment to relax completely. By adding this shaking technique to the MO system we extended the regions of the H-T phase diagram in which MO measurements can be done at equilibrium conditions.

4.3 Artificially introduced disorder

To study the dynamics and thermodynamics of the vortex matter in the presence of disorder, we introduced limited regions with artificial pinning centers in our samples. This was done by irradiating the samples through appropriate masks to produce adjacent irradiated and non-irradiated regions

in the same crystal. This patterning allows sensitive comparison of the vortex structure and the phase transitions in adjacent irradiated and pristine regions. The introduction of CDs, extending through the sample, was introduced by heavy ion irradiation. In this study we produced CDs that are tilted with respect to the c-axis. Tilting the field relative to the direction of the CDs was found to weaken the pinning strength of the CDs [61]. This tilting together with the ability to tilt the applied magnetic field, provides an additional degree of freedom to the vortex system, in which one can control the pinning force by changing the angle between the CDs and the applied magnetic field.

4.4 Hall Sensor measurements

The understanding of the tunneling of the magnetization in single molecule magnet is based largely on the results of magnetization measurements, in which the magnetic response to an externally applied field is measured. Most of the magnetization measurements are global measurements, in which the integrated magnetic response of the entire sample is measured by magnetic sensors (e.g. SQUID). These measurements provide the magnetic induction as averaged over the whole sample. As such, these measurements do not provide any information on the spatial profile of the magnetization in the sample or on how the relaxation process propagates spatially within the sample. In this work, we use a local Hall sensor array technique that was developed in our lab [29]. This technique uses an array of two-dimensional electron gas (2DEG) Hall sensors, manufactured using well-established photolithographic and etching techniques. These sensors, which can be manufactured with small dimensions of down to 1x1μm^2, have the advantage of a linear response to a magnetic field, weak temperature dependence, and high sen-

sitivity. In this technique, the sample is mounted onto the surface of the array. A current is driven through all the sensors and the corresponding Hall voltage of each sensor is directly proportional to the perpendicular component of the local magnetic field within the active area of the sensor. This technique allows a very sensitive mapping of the local magnetic field across the sample.

5. EXPERIMENTAL SETUP FOR MAGNETO-OPTICAL MEASUREMENTS

5.1 The cryogenic system

The optical cryostat is a modified RC102 continuous flow cryostat manufactured by CRYO Industries of America. The cryostat is made of stainless steel and has an inner cold part made of copper and surrounded by an Aluminum radiation shield. A heater and AlGaAs temperature sensor are mounted at the end of the cold part near the sample space. The home-made cold finger extends above the plane of the cryostat and into the tube of the cover lid. The samples are mounted in the center of a vector electro-magnet. A 44-pin chip carrier socket is mounted at the top of the cold finger and wired to two standard 26-pin connectors. This enables performing simultaneous MO and transport or Hall sensor measurements. The wires are wound around the cold finger and the cold part of the cryostat in order to reduce thermal coupling. The cover lid is also home-made and has a central tube that surrounds the cold finger. A fused silica window with AR coating manufactured by VLOC is mounted on the top of the lid tube using an O-ring and a clamp.

We used a standard helium storage vessel containing 110 liters, which allows up to five days of continuous measurements. The helium is transferred to the cryostat using a transfer line that exits through a flow meter into the helium recovery line. The flow meter is equipped with a control valve, which

allows a fine tuning of the helium flow in addition to the main valve of the transfer tube. A steady helium flow is achieved by keeping the gas pressure in the vessel on a level of 3-5 psi, which is maintained by a pressure release valve connecting the vessel to the recovery line. The helium flow is kept constant during the measurement and is monitored by the flow meter. The temperature of the cryostat and the MO sample holder were controlled by a LakeShore340 temperature controller.

5.2 Microscope

We use a commercial Leica DMR microscope designed for work with polarized light. The objectives ($\times 2.5$, $\times 5$ and $\times 10$) are objectives for polarized light which were specially inspected to be strain-free and have a long-working distance. The beamsplitter is a Smith prism, which gives optimal extinction for the vertical or horizontal polarization of the incident light. The microscope is equipped with two light sources - a halogen lamp and a mercury lamp, which is controlled by a stabilized power supply. All the measurements are performed with the mercury lamp, which has strong radiation lines in green. The microscope is equipped with three green filters of different bandwidth and a hot mirror which blocks the UV and IR radiation and protects the polarizer and the optics.

5.3 CCD camera

The camera is a Photometric Quantix 57 frame transfer camera with a maximal frame readout of 10 frames per second. The ccd chip has an imaging area of 535×512 pixels with a pixel size of $13 \times 13 \mu m^2$. The image is digitized by a 12-bit analog to digital converter located on the chip and transferred by a

data cable with 68 pin connectors to the computer.

5.4 Vector magnet

The vector magnet is composed of three coils contained in a stainless steel case allowing the application of a magnetic field in any desired direction. The coils are made of copper wires coated by polyamid-imide coating with current responses of 14.8 G/A for the z (out of plane) coil and 14.7 G/A for the in-plane x and y coils. The coils were water cooled by a QUANTRONIX cooler which enables the performance of long measurements with magnetic field of up to 250 Oe in each coil, without substantial heating of the coil. The z coil is driven by a dc current, supplied by a BOP 36-28MG Kepco power supply which in turn is controlled by a Yokogawa 7651 voltage source. The in-plane x and y coils are driven by either dc or ac currents, supplied by a BOP 36-28MG Kepco power supply. The BOP is controlled by an Agilent 8904a multifunction synthesizer. The default applied shaking field has an amplitude of 250 Oe and a frequency of 15 Hz.

5.5 Data acquisition and data analysis

The instruments and camera are controlled using a LabView program through a GPIB interface or by calling a DLL (camera). All measurements are carried out automatically by executing LabView programs, namely the experiments may perform over several days without a need for human intervention. The acquired MO images are saved as 16-bit TIF files. Data analysis was done using Matlab.

6. EXPERIMENTAL SETUP FOR LOCAL MAGNETIZATION MEASUREMENTS

6.1 Cryogenic system

An Oxford Research instrument He^3 cryostat was used to cool the sample and detector down to 250 mK temperatures. Mounted withing the liquid He^4 is a 12T superconducting coil manufactured by Cryogenics. A stainless steel He^3 insert is mounted in the center of the superconducting coil. A rotatable probe containing Ruthenium Oxide thermometer and a home made detector assembly unit are inserted within the He^3 insert. Temperature stabilization was achieved by a feed-back loop using a secondary thermometer placed outside the superconducting coil and thus unaffected by the magnetic field.

6.2 Local magnetization measurements

To measure the magnetization of the sample, the sample is mounted with the easy c-axis of the crystal aligned parallel to the surface of the detector and the applied magnetic field, as shown schematically in Fig. 6.1. As the sample becomes magnetized the field lines of the sample penetrate the active area of the Hall sensors. If the Hall sensors array is mounted exactly parallel, there will be no signal from the external field. Any signal will then be entirely due to the sample.

The sensors were made from two-dimensional electron gas (2DEG) formed

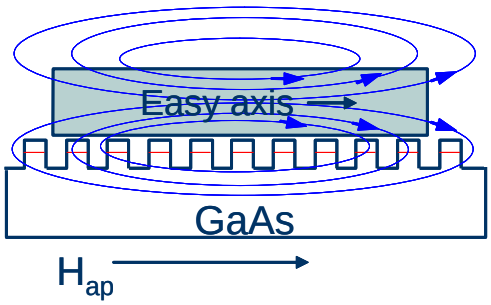

Fig. 6.1: The experimtal setup used to measure the magnetization across the Mn_{12} sample.

at a GaAs/AlGaAs interface. The 2DEG active layer resided only 1000 Å below the surface, resulting in a very accurate measurement of the local magnetic field at each of the sensor locations across the sample. The 2DEG usually has a mobility of about $1 \times 10^5 \text{cm}^2/\text{Vsec}$ at 80 K and a density of about $6 \times 10^{11} \text{cm}^{-2}$ resulting in a sensitivity of about 0.1 Ω/Gauss. In the DC magnetization measurements, a 50 μA Hall current was driven through the sensor array and the Hall voltage was measured using a HP34401A digital voltmeter. All the sensors in the array were measured one after the other for each temperature and field by switching the voltmeter connection to each sensor, using a Keithley 7001 switch system.

7. RESULTS AND DISCUSSION

7.1 Dynamic and thermodynamic properties of porous vortex matter in $Bi_2Sr_2CaCu_2O_8$ *in an oblique magnetic field*

The dynamic and thermodynamic properties of vortex matter in high T_c superconductors are strongly affected by the introduction of correlated disorder in the form of CDs. In the presence of a low concentration of CDs, experimental [42, 43, 44] and theoretical results [45, 46, 47, 48, 49, 50] indicate the presence of two vortex subsystems: vortices localized on pinning centers and interstitial vortices between them. At low temperature, a *porous vortex solid* phase is created. A rigid matrix of vortices, strongly pinned on a network of random CDs, is formed, while the interstitial vortices create relatively ordered nanocrystals within the pores of the matrix. When the temperature is increased, the interstitial vortices melt while the rigid matrix remains localized, forming a *nanoliquid* phase in which nanodroplets of liquid are weakly confined within the pores of the matrix. When the temperature is increased further, the matrix delocalizes at the delocalization transition, and the liquid becomes *homogeneous*. Above this transition the effect of the CDs on vortex dynamics becomes indiscernible.

This picture holds when the angle θ between the average induction $\mathbf{B}$ and the CDs is zero. According to theoretical models [2, 62], for small θ, the localized vortices on CDs remain completely trapped along the CDs. At larger

θ, the vortices form a staircase structure with segments trapped on different CDs connected by weakly pinned kinks. At still larger angles, the vortices follow the field direction and are not affected by the correlated nature of the CDs. In general, one expects the effect of the correlated nature of the CDs to decrease as θ increases, and to vanish at $\theta = 90°$. In more isotropic materials such as $YBa_2Cu_3O_7$, this picture is supported by various experiments, showing an angle dependent behavior in both dynamic [63, 64] and thermodynamic [65] properties. In layered materials such as BSCCO, vortices consist of stacks of two-dimensional pancake vortices (PVs) defined in the superconducting CuO_2 layers only. Measurements of the equilibrium torque and magnetization in BSCCO [66] have shown that the CD occupation by PVs in the liquid phase is angle independent. In contrast, Josephson plasma resonance measurements [67] show that the PV alignment in the liquid is significantly affected by CDs. The corresponding equilibrium properties of the solid phase have not been studied. Since the melting transition depends on the difference in the behavior of the free energies of the solid and liquid, it is very interesting to study the angular dependence of the melting in the presence of CDs. Moreover, CDs are known to shift the first-order melting line upward [42] and point disorder was found to shift it downward [35]. One might expect, therefore, that tilting $\mathbf{B}$ away from the CDs would shift the melting line continuously from above the pristine melting line to below it, reaching the lowest position at $\theta = 90°$, where CDs act like point defects.

Here, we study the angular dependence of the dynamic and thermodynamic properties of porous vortex matter in BSCCO. Our measurements show that the irreversibility line shifts to lower T when the field is tilted away from the CDs, as expected [63, 68, 69, 70]. However, the thermodynamic melting and delocalization lines have *no* angular dependence. Our

simulations show that even at large angles the PVs are effectively pinned by the CDs and therefore the thermodynamic features remain unaffected. On the other hand, the formation of a kink structure of the PV stacks increases their mobility due to kink sliding, therefore suppressing the irreversible properties.

For the measurements, BSCCO crystals ($T_c \approx 90$ K) were irradiated, at GANIL, with 1 GeV Pb ions, through stainless steel masks with triangular arrays of 90 μm holes. This produces amorphous columnar tracks, with density n_d equal to the ion dose, only in those parts of the crystals situated under the holes. Crystals A and B, irradiated at 45° with respect to the c-axis, have matching fields $B_\phi = n_d\Phi_0$ of 20 G and 30 G respectively. The measurements were performed using differential DMO [57] with a vector magnet that allows application of a DC magnetic field in any direction, so that the local magnetic response can be imaged over the full range of angles from $\mathbf{B} \parallel$ CDs ($\theta = 0$) to $\mathbf{B} \perp$ CDs ($\theta = 90°$).

Figure 7.1a shows the irreversibility line of the irradiated regions $H_{irr}^{cd}(T)$ on an $H_z - T$ plane, where H_z is the c-axis component of the applied field, for different angles of $\mathbf{B}$ with respect to the CDs [71]. The curves were obtained using DMO with field modulation of 1 Oe, upon sweeping the temperature. Below $H_{irr}^{cd}(T)$, the external field modulation is shielded in the irradiated regions due to enhanced pinning [42]. Hence, the dark regions in the DMO image (Fig. 7.1b) are the irradiated regions, while the bright background is the reversible pristine region. Upon increasing T, these dark regions gradually fade until they disappear completely at $H_{irr}^{cd}(T)$, where the screening current drops to an unobservably low level.

Figure 7.1a shows that upon tilting the field away from the CDs (changing θ from 0 to 90°), the irreversibility line shifts to lower temperatures. For

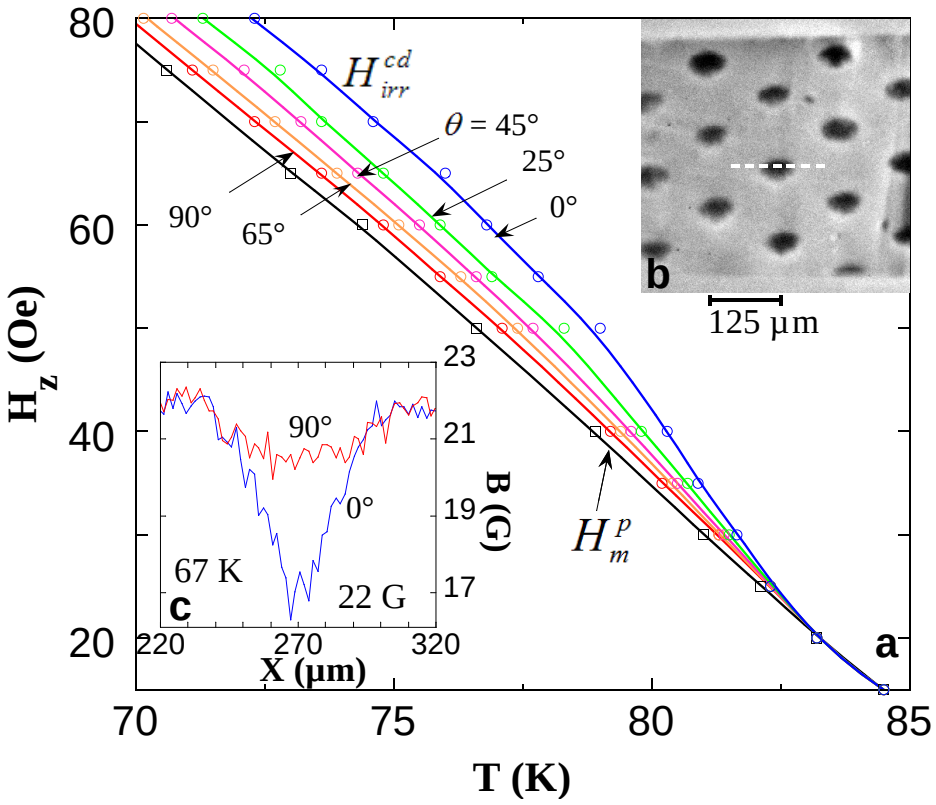

Fig. 7.1: (a) The irreversibility line $H_{irr}^{cd}(T)$ of crystal A, mapped for five angles θ between **B** and the CDs, from $\theta = 0$ to 90°. H_m^p is the pristine melting line. (b) DMO image of part of the sample at $T = 79$ K and $H_z = 35$ Oe. (c) Flux profiles across the irradiated region [dashed line in (b)], at 67 K and $H_z = 22$ Oe, for $\theta = 0°$ and 90°.

example, at $H_z = 70$ Oe the irreversibility temperature at 90° is 2.5 K lower than at $\theta = 0$. Even at $\theta = 90°$, $H_{irr}^{cd}(T)$ remains slightly above the melting line of the vortex lattice in the pristine crystal, $H_m^p(T)$. This is at odds with the expectation that at $\theta = 90°$ the CDs act as weak point disorder; then, the melting and irreversibility lines are expected to lie below $H_m^p(T)$ [35]. The angular dependence of $H_{irr}^{cd}(T)$ is more pronounced at lower temperatures. It decreases upon increasing T until it disappears completely at ~ 82 K, above

which all lines coincide with $H_m^p(T)$. This behavior was observed for different samples with B_ϕ of 20, 30 and 40 G. The relative shift in $H_{irr}^{cd}(T)$ between $\theta = 0$ to 90° was found to increase with B_ϕ.

To examine the vortex behavior below $H_{irr}^{cd}(T)$, within the vortex solid phase, we performed conventional MO measurements, in which a sequence of images is taken while the applied field H_a is swept. Figure 7.1c shows flux profiles across the irradiated regions. These have a linear (Bean-like) shape due to the enhanced pinning in these regions. The profiles were taken at $H_z = 22$ Oe and $T = 67$ K, well below $H_{irr}^{cd}(T)$. At $\theta = 90°$, the profile is very shallow. In contrast, at $\theta = 0$, a clear sharp profile is observed. The critical current, estimated from the flux gradient, is 3.5 times higher at $\theta = 0$ than at 90°.

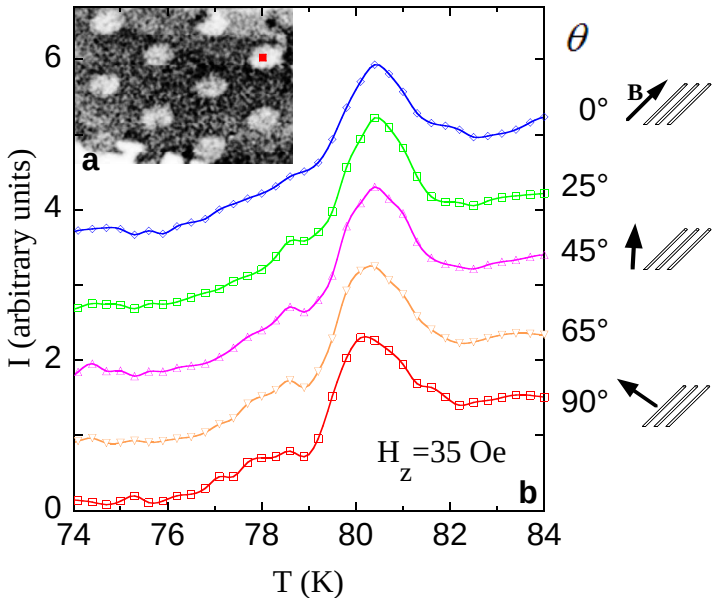

Fig. 7.2: The melting transition in crystal B. (a) DMO image of part of the sample at $H_z = 35$ Oe, $T = 81$ K. (b) Local DMO intensity versus T for different angles θ. The peak around 80.4 K corresponds to the melting transition. The curves are vertically displaced for clarity.

The angular dependence of the melting transition was studied using DMO upon temperature sweeps with T modulation [57, 42]. The first-order melting transition is characterized by a step in the equilibrium flux density, and appears as a bright signal in the DMO images. For example, the bright circular regions in Fig. 7.2a are the irradiated areas that undergo melting, while the surrounding pristine regions are already in the liquid phase and hence appear as a darker background.

Figure 7.2b shows the local DMO intensity, averaged over a region of 15×15 μm^2 in one of the irradiated regions (red square in Fig. 7.2a). The melting transition manifests itself as a peak in the local intensity as T is swept. Each curve corresponds to a different θ, while $H_z = 35$ Oe was kept constant. In contrast to the irreversibility line that shifts to lower T upon increasing θ, the melting temperature remains unaffected, even when $\mathbf{B}$ is perpendicular to the CDs. Moreover, the transition width, determined from the width of the peak, appears to be the same for all measured angles. Similar results were obtained for different H_z values. Note that the pristine melting line was found to have a weak linear dependence on the in-plane field [72, 73] which cannot be detected within our experimental resolution for our low in-plane fields.

Fig. 7.3a gathers the melting lines obtained at different angles θ. They all fall on a single line, $H_m^{cd}(T)$, that terminates at a critical point (CP) below which the transition becomes continuous in nature. The CP occurs at the same temperature of 77 K at all angles. The width of the transition, denoted by the horizontal right-pointing arrows, is broadened on approaching the CP, but remains independent of angle, as was already shown in Fig. 7.2 for $H_z = 35$ Oe. In Fig. 7.3, we also plot the delocalization line $H_{dl}(T)$ [43], which separates the nanoliquid from the homogeneous liquid. $H_{dl}(T)$ was

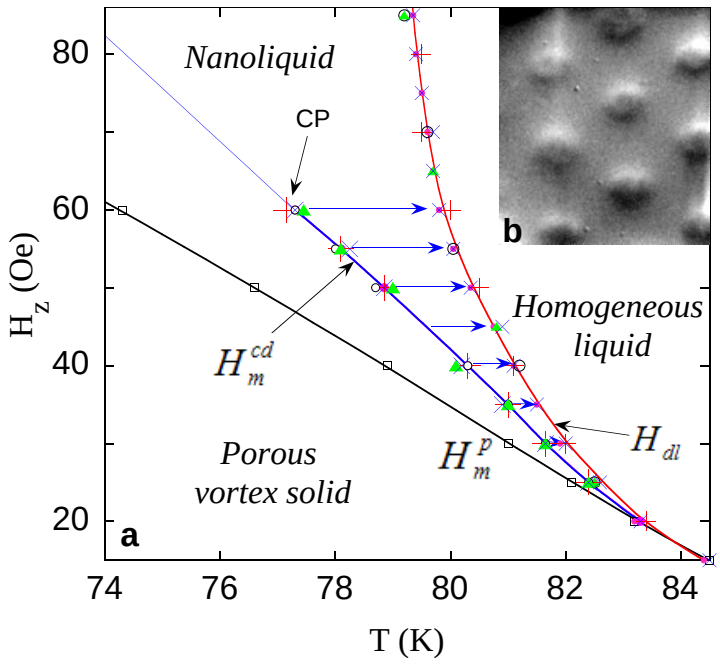

Fig. 7.3: (a) The melting line $H_m^{cd}(T)$ and the delocalization line $H_{dl}(T)$ in crystal A, mapped for different θ: 0(+), 25°(○), 45°(●), 65°(▲) and 90°(×). (b) DMO self- field image of part of sample A at 40 Oe, 75 K, 20 mA.

determined using MO visualization of the self-field induced by a transport current applied to the sample. DMO image of the self-field allows one to visualize the transport current density distribution within the sample. Below $H_{dl}(T)$, the current flow is highly nonuniform due to enhanced pinning in the irradiated regions [43], and the DMO image shows significant spatial variations (Fig. 7.3b). These disappear at H_{dl}, when the network of pinned vortices is delocalized, and a homogeneous liquid is formed. As $H_m^{cd}(T)$, the $H_{dl}(T)$ does not depend on the field angle θ (Fig. 7.3a). On approaching T_c, vortex pinning by CDs becomes weak and hence all the transition lines coincide.

The experimental observations show that the dynamic properties of porous vortex matter are strongly dependent on the angle between **B** and the CDs,

while the thermodynamic melting and delocalization lines are angle-independent. In order to understand these observations, we have carried molecular dynamics simulations of a rectangular parallelepiped model system of 36 PV stacks and 200 layers. As shown in [50, 74], such system size is sufficient for observing the various phase transitions. Periodic boundary conditions (PBC) were implemented in all directions. The intraplane PV interaction was modeled by the repulsion of their screening currents, while the interplane PV interaction is described by their mutual electromagnetic attraction [50, 75, 76, 77]. We also included the attractive Josephson interaction between pairs of pancakes in adjacent planes, but belonging to the same stack [75, 76, 77]. We keep track of pancakes belonging to a vortex stack and allow for flux cutting and recombination [75, 76, 77]. The average vortex direction (i.e. H_a) was kept parallel to the z axis, while tilted CDs of radius $r_r = 30$ nm were introduced at random positions. The interaction between a pancake and a CD in the same plane is given by an attractive potential [2, 50], which has a long range tail contribution $\approx -\epsilon_0 d r_r^2/R^2$, due mainly to the electromagnetic pinning, and a short range flat region of depth $\approx \epsilon_0 d$ due to the combined effects of electromagnetic and core pinning. Here, $\epsilon_0 = (\phi_0/4\pi\lambda)^2$, $\lambda = \lambda(0)/(1-T/T_c)^{1/2}$ is the penetration depth, R is the distance between a pancake and a CD and d is the layer separation. The interaction $-\mathbf{B}\cdot\mathbf{H}/(4\pi)$ is implemented by the PBC, since the electromagnetic interaction between a tilted stack and the stacks of images, positioned above (and below) its center of mass, pull the tilted stack in the z direction. Temperature effects are implemented in the simulation by using a white thermal noise whose variance is proportional to the temperature.

Figure 7.4 shows projections of the vortices onto the xy plane (top view) and the xz plane (side view), with CDs tilted by 45° and 80°. The main

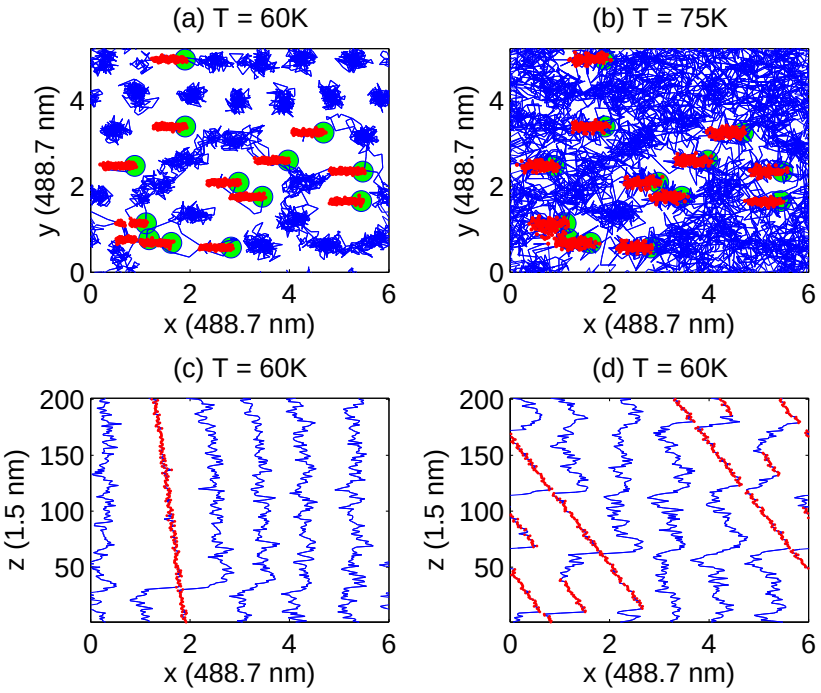

Fig. 7.4: Snapshots of vortex stacks and CDs tilted at 45°(a, b and c) and 80°(d) for $B = 100$ G and $B_{\phi}^{eff} = 35$ G. Pancakes in the same stack are connected. Free pancakes are in blue, trapped ones in red. Only CDs at the bottom layer are shown (green). (a)(b) Projection onto the a-b plane (top view). (a) Nanosolid phase. (b) Nanoliquid phase. (c) Projection of (a) onto the a-c plane (side view), first row is shown. (d) Side view with CDs at 80°.

observation is that, for $B > B_\phi$, the CDs are almost fully decorated by pancakes both in the solid and nanoliquid phases. This means that the matrix of pinned PVs is preserved even when the field is tilted away from the CDs, and as a result the interstitial PVs remain caged in the surrounding fixed matrix. The interstitial PV stacks are even found to be tilted to some extent in the direction of CDs, in the solid phase. Another important observation is that the vortices adopt a structure featuring kinks between the layers, as shown by the side views in Figs. 7.4c and 7.4d. Kinks of different vortices tend to align, forming a structure which resembles the Josephson and Abrikosov crossing lattices [59] in BSCCO at tilted field. Here, however, the Josephson vortices (JV) are formed when tilting the field away from CDs rather than from the c-axis. For example, when $\mathbf{B}$ is parallel to the CDs but at 45° with respect to c-axis, no JVs are present, while for $\mathbf{B} \parallel c$-axis JVs segments appear, as shown in Figs. 7.4c and 7.4d.

To further interpret the results we consider the energies involved: The binding energy of a vortex to a CD is of the order of $\epsilon_0 d$ per layer. For angles less than about 75° this gain exceeds the electromagnetic energy loss. For an infinitely long stack tilted at angle θ, the later is given by $\epsilon_0 d \ln((1+\cos(\theta))/2\cos(\theta))$ per layer [78]. In addition, the energy $-\mathbf{B}\cdot\mathbf{H}/(4\pi)$ tends to align the average vortex orientation with $\mathbf{H}$. The contradicting requirements imposed by the need to minimize all these energies are optimized by the creation of kinks. The Josephson energy cost of the kinks is negligible compared to the total energy of the vortex system in a highly anisotropic material like BSCCO [79]. Indeed, for $\gamma \sim 375$, the total energy measured in the simulations for non tilted CDs and for CDs tilted at 45° is the same, in the vicinity of the melting transition ($T = 73$ K to 77 K), within the simulation's error bars. The comparison was done for the same value of $B_\phi^{eff} = B_\phi \cos\theta$

in order to match the experimental situation where the ratio of vortices to CDs remains fixed as θ changes. Our simulations show that the rigid matrix of pancakes pinned on CDs is preserved up to very large angles in both the solid and nanoliquid vortex phases. This means that the enhanced caging potential created by the CDs, that was found to shift the melting line upwards, [42] is negligibly affected by increasing the angle between $\mathbf{B}$ and the CDs. Consequently, the thermodynamic properties, in particular the melting and delocalization lines, are angle independent. This was verified in our simulations for $B = 100$ G, where the melting and delocalization transitions occur at 74 K and 76 K respectively, both for nontilted and tilted CDs, as evidenced by measurements of the mean square deviation of the flux lines, the amount of their entanglement and other measurements [80].

These observations can resolve the apparent discrepancy between the dynamic and thermodynamic properties. The kinks developed by the vortices have a negligible effect on the thermodynamics but a large effect on the dynamics. As demonstrated by our simulations, the kinks slide along the CDs due to the Lorentz force exerted by in-plane current, see also [62, 81, 82]. Consequently, they transfer PVs between segments, thus producing an effective transverse drift of the whole pancake stack. Upon increasing θ, the amount of kinks increases and the flux creep becomes more effective. This process decreases the critical current and shifts the irreversibility line to lower temperatures. This is consistent with [66], which concluded that CDs' pinning anisotropy commonly measured in BSCCO [68, 69, 70] must be a dynamic effect.

In summary, the porous vortex matter in BSCCO is shown to preserve its thermodynamic properties even when the field is tilted away from the CDs. While the irreversibility line shifts to lower temperatures upon tilting the

field, the thermodynamic melting and delocalization lines remain constant. Numerical simulation shows that increasing the angle between the field and the CDs leads to formation of weakly pinned vortex kinks, while preserving the basic structure of a rigid matrix of pancake stacks residing along the CDs with nanocrystals of interstitial vortices embedded within the pores of the matrix.

7.2 The effect of spatial variations in the lower critical field on field penetration into superconductors

The thermodynamic lower critical field H_{c1} is one of the fundamental parameters of the mixed state in type II superconductors. At H_{c1} the formation of vortices becomes energetically favorable and the superconductor undergoes a transition from the Meissner state to the mixed state. The value of H_{c1} and the way the field penetrates into the sample are directly related to the free energy of a vortex and to essential mixed state parameters such as the penetration depth λ and the Ginzburg-Landau parameter κ.

Experimentally, one measures the penetration field H_p which differs from H_{c1} due to demagnetization effects which cause distortion of the external field. Due to this distortion the local field at the sample edges can be significantly higher than the applied field H_a and therefore field penetration occurs at H_p which is substantially smaller than H_{c1}.

An additional major difficulty in determining H_{c1} and moreover in measuring small variations in H_{c1}, is the energy barriers against vortex penetration which hinder the system from reaching thermodynamic equilibrium. A major contribution to the hysteresis comes from geometrical [83, 84, 85] and surface [86, 87] barriers. The geometrical barrier arises from the competition between the inward Lorentz force due to the Meissner shielding currents and the outward force due to increase in vortex line energy. The surface barrier arises from the competition between the attraction of vortices to the sample's surface and the inward repulsion due to Meissner currents flowing at the surface. In addition, bulk pinning delays vortex penetration into the sample resulting in a Bean critical state. As a consequence of the edge barriers and pinning, all studies of the phase transition at H_{c1} must contend

with irreversibility and hysteresis. Most of the previous experimental works [88, 89, 90], therefore, studied the transition at H_{c1} by investigating the thermally activated penetration of vortices through the energy barriers and by the way this process is influenced by different kinds of disorder.

In the present study we aim at obtaining a more accurate determination of the thermodynamic H_{c1} and to investigate how small variations in H_{c1} affect the way the field penetrates into superconductors. To overcome the non-equilibrium conditions hindering the detection of the thermodynamic behavior, we use vortex shaking technique [36, 58] in which an in-plane ac field is used to 'shake' the vortices towards their equilibrium state. The in-plane ac field generates dissipation [91, 92, 93] in the sample that causes the critical current to relax completely. This enables measuring the equilibrium properties of the vortex matter even in the presence of strong pinning [36, 37].

In order to form controlled spatial variations in H_{c1} we irradiated the sample to create columnar defects in specific regions. The introduction of CDs is expected to decrease the free energy of a vortex line [94, 95, 96, 97] and consequently to reduce H_{c1} [2, 98, 99, 100]. CDs are very effective in pinning vortices when oriented along the field direction and are usually used to enhance pinning [63, 64, 101, 102]. Here, however, we use them for the purpose of reducing H_{c1}. The unwanted pinning is then removed by shaking.

We used differential magneto-optical measurements [103] combined with the shaking technique to study the equilibrium field penetration into BSCCO crystals containing small regions with CDs. We observe an unexpectedly large variation in H_p between the irradiated and pristine regions and a remarkably abrupt field penetration which leads to a paramagnetic local magnetization in the irradiated regions. We derive a theoretical model which explains how, in the presence of large demagnetization effects, a small vari-

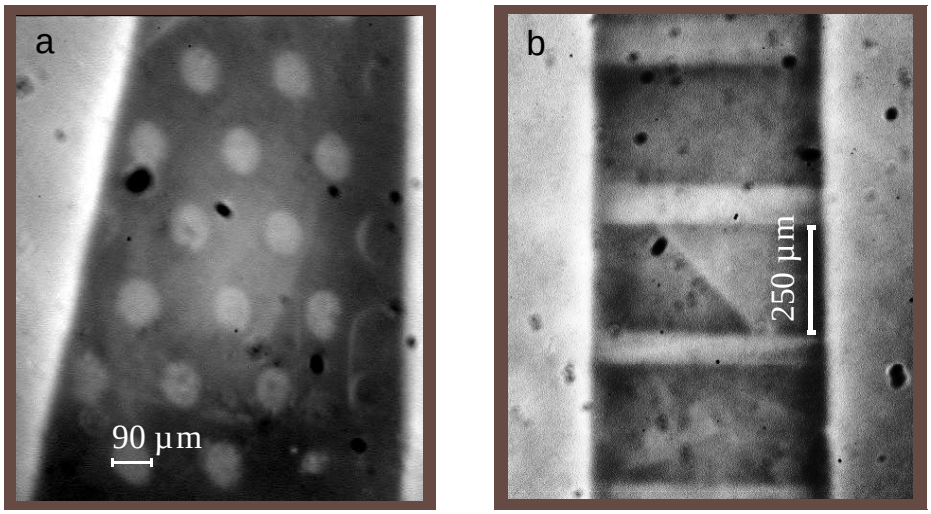

Fig. 7.5: Magneto-optical images of crystals A and B in presence of shaking. (a) Crystal A ($0.92 \times 1.5 \times 0.04$ mm^3) at 62K, the white circles show the enhanced flux in the irradiated regions. (b) Crystal B ($0.57 \times 1.2 \times 0.04$ mm^3) at 64 K, the white strips show the irradiated regions.

ation in H_{c1} can lead to significantly larger variations in the local H_p. The model also accounts for the observed positive local magnetization and provides a quantitative fit to the experimental data.

The measurements were performed on several BSCCO crystals ($T_c \approx$ 90K) irradiated at GANIL by 1 GeV Pb ions. The crystals were covered with masks prior to irradiation in order to produce the CDs, with density n_d equal to the ion dose, only in specific regions. This allows a sensitive comparison between irradiated and non-irradiated regions located in proximity to one another. The comparison between neighboring regions avoids possible differences in vortex behavior on larger scales arising from intrinsic inhomogeneities of the sample. A dc magnetic field H_a was applied parallel to the crystalline c axis, while an ac transverse field H_{ac}, with frequency of 10 Hz and an amplitude up to 230 Oe, was applied along the a-b planes. We present

here results for two crystals irradiated through masks of different geometries: crystal A with matching field $B_\phi = n_d\Phi_0$ of 30 G, where n_d is the density of CDs and Φ_0 is the flux quantum, was irradiated through a stainless steel mask with a triangular array of 90 μm holes (Fig. 7.5a). Crystal B, with $B_\phi = 200$ G was irradiated through a mask of gold strips, resulting in the formation of alternating irradiated and non-irradiated strips (Fig. 7.5b).

The suppression of the hysteresis by applying an in-plane ac field is demonstrated in Fig. 7.6, for both the pristine (Fig. 7.6a) and the irradiated (Fig. 7.6b) regions. Each figure shows two local magnetization loops $B - H_a$ at 73 K with and without shaking. The curves were obtained using conventional magneto-optical measurements, in which a sequence of images is taken upon sweeping H_a. Without H_{ac}, a hysteretic behavior is observed in the pristine region and a larger hysteresis, due to enhanced pinning by CDs, is seen in the irradiated regions. Applying an ac field allowed us to suppress the hysteresis in both the pristine and the irradiated regions and to obtain fully reversible curves, as shown by the red curves in Figs. 7.6a and 7.6b. These reversible curves enable the determination of H_{c1}, and the investigation of the transition from the Meissner state to the mixed state in equilibrium conditions.

Figure 7.7 presents a sequence of DMO images from a movie [104] of the transition from the Meissner state to the mixed state under equilibrium conditions upon sweeping H_a at 72 K. A DMO image is obtained by taking the difference between the MO images at $H_a+\delta H_a$ and $H_a-\delta H_a$ and averaging a large number of such differential images [103]. An abrupt change in the local density of the vortices appears as a bright feature in the DMO image. In Fig. 7.7a both the irradiated and the pristine regions are in the Meissner state, therefore, no change in the vortex density is detected upon field modulation

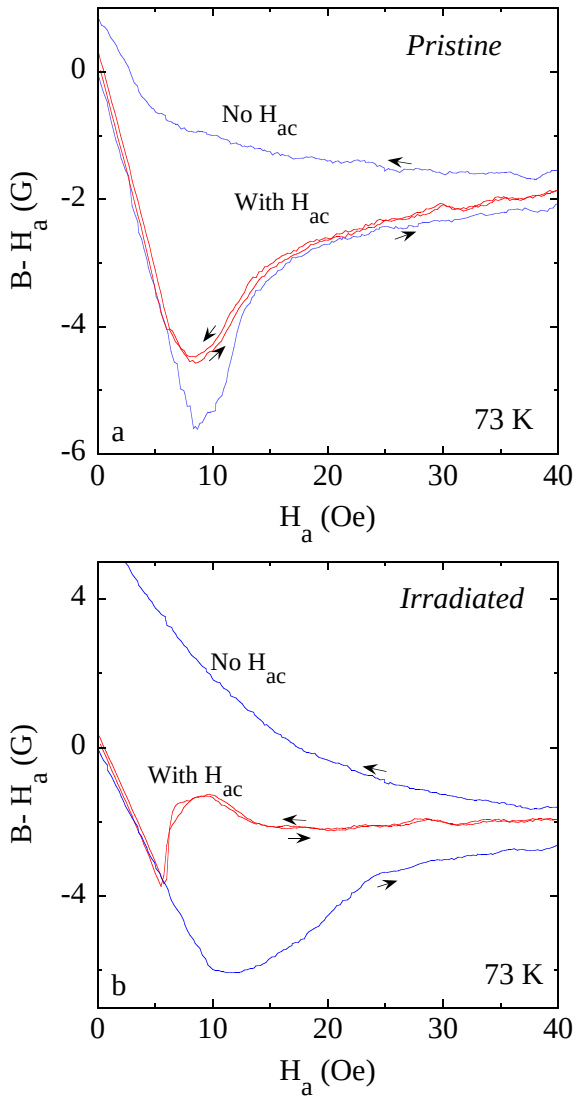

Fig. 7.6: Suppression of the hysteresis by an in-plane ac field in crystal A. (a) Local magnetization loops with H_{ac} (red) and without H_{ac} (blue) measured in the pristine region. (b) Same as (a) for the irradiated regions.

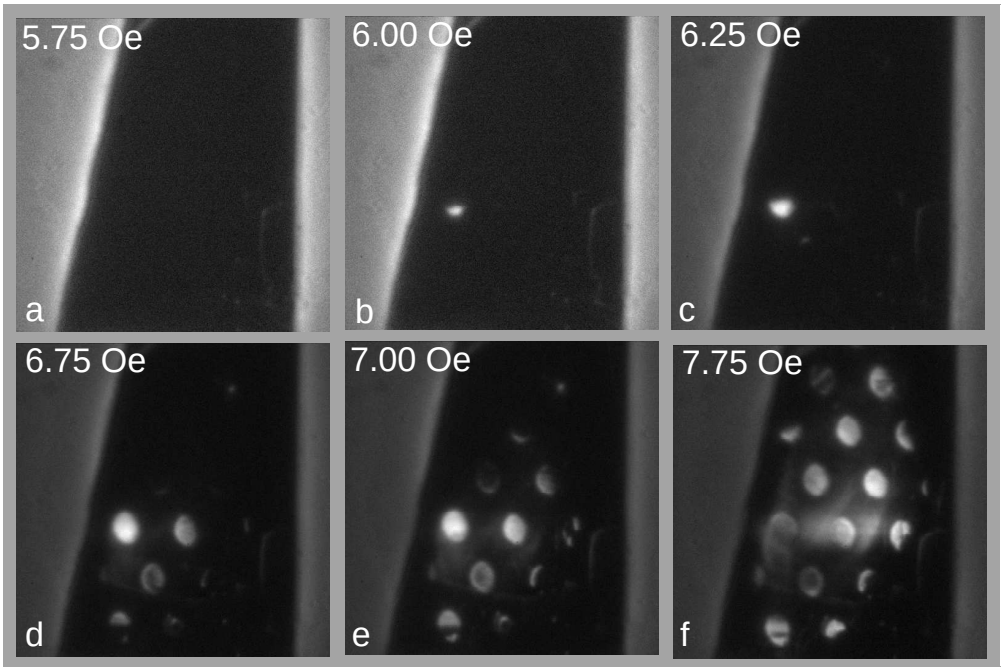

Fig. 7.7: A sequence of images from a movie of the transition from Meissner to mixed state in crystal A at 72 K in presence of shaking. At $H_a = 5.75$ Oe the sample is still in the Meissner state (a). At 6 Oe, vortices start to penetrate into one of the irradiated regions (b). In (c), (d) and (e) the vortices penetrate into additional irradiated regions but the pristine region is still mostly in the Meissner state. At 7.75 Oe the vortices penetrate also into the pristine region.

and the whole sample appears dark. When increasing H_a to 6 Oe, a bright region appears in one of the irradiated regions in the left part of the sample, indicating the penetration of vortices into the irradiated region. When further increasing the field, more vortices penetrate into this region while the surrounding pristine regions are still in the Meissner state. In Figs. 7.7d and 7.7e the vortices penetrate into additional irradiated regions. Due to intrinsic inhomogeneity of the sample and geometrical effects, however, the

field does not penetrate simultaneously into all the irradiated regions. Yet it is clear that throughout the sample, the field penetrates first to the irradiated regions and only later to the adjacent pristine areas. Finally, at 7.75 Oe the vortices penetrate also into the pristine regions as shown by the bright region in the middle of the sample. Note that in crystal A the irradiated regions are surrounded completely by pristine region. Naturally, vortices are not expected to penetrate into the irradiated regions below H_{c1}^{p} of the surrounding pristine region. However, due to the high anisotropy of BSCCO, Josephson vortices arising from the in-plane shaking field can penetrate the sample at vanishingly low fields. Consequently, vortices can accumulate in the irradiated regions once H_{c1} of the irradiated regions is exceeded.

In order to compare the penetration of vortices into the irradiated vs. pristine regions, we plot, in Fig. 7.8a, the equilibrium local magnetization curves for adjacent irradiated and pristine regions. The curves were extracted from a movie of conventional MO measurement by averaging over regions of 15×15 μm^2 each. The reduction in the penetration field H_p due to CDs is clearly shown. For a temperature of 68 K in crystal B, the penetration field of the irradiated regions H_p^{cd} is 2.8 Oe lower than H_p^p of the pristine region. Another example is shown in Fig. 7.8b for crystal A, at a temperature of 72 K. H_p^{cd} in the irradiated regions is 2.7 Oe lower than H_p^p measured in the pristine region. To the best of our knowledge, this is the first unambiguous observation of reduction of H_{c1} by CDs.

The second important observation in Fig. 7.8a is the remarkable difference in the behavior of the magnetization in the irradiated and in the pristine regions near the penetration fields. In the pristine region, a gradual increase in flux density is observed when the penetration field $H_a = H_p^p$ is exceeded. In contrast, in the irradiated regions, a sharp discontinuity in

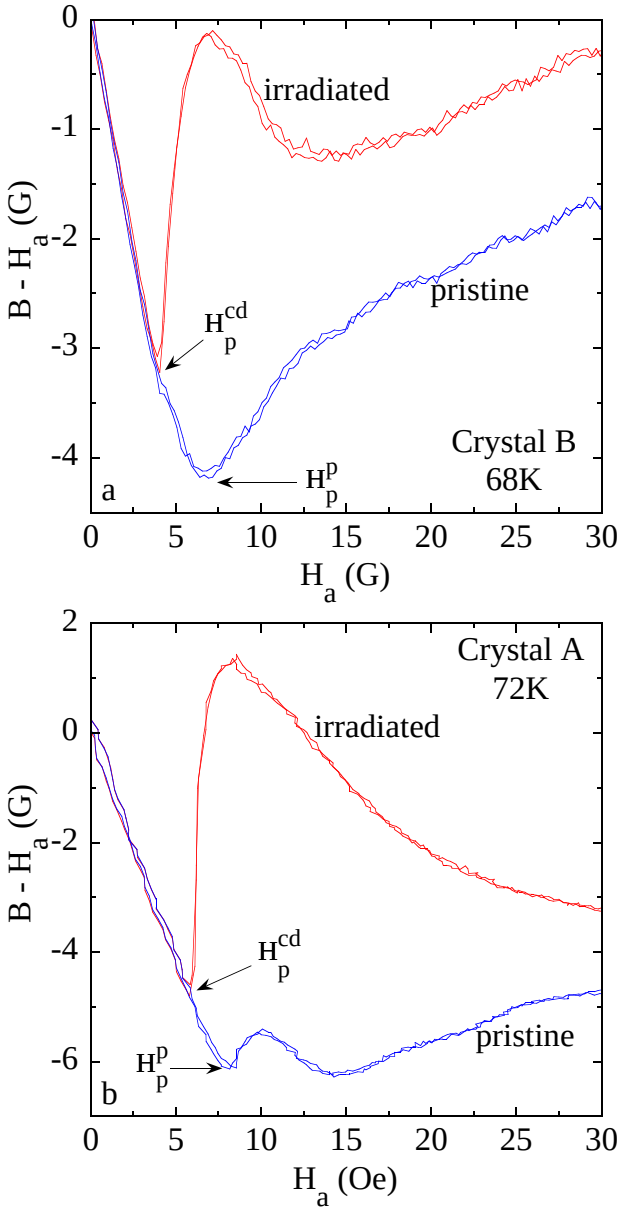

Fig. 7.8: (a) Two local magnetization loops measured in adjacent pristine (blue) and irradiated (red) regions, in crystal B, at 68 K, in presence of shaking. (b) Two local magnetization loops in crystal A, at 72 K. The curves were measured while sweeping H_a in steps of 0.15 Oe. Note that in the irradiated region in (b) the local magnetization at the peak is positive.

flux density appears at H_p^{cd} in both increasing and decreasing branches of the magnetization curve. This is even more pronounced in Fig. 7.8b where the local magnetization in the irradiated regions increases abruptly from a negative value in the Meissner state to a positive value above penetration. This means that the induction B in the irradiated regions becomes larger than H_a. When further increasing H_a, the magnetization in the irradiated regions starts decreasing and eventually approaches the magnetization of the pristine region. We note that the curves are reversible and therefore describe the thermodynamic behavior of the system. The second dip observed around 14 Oe in the local magnetization of the pristine region in Fig. 7.8b, apparently results from some inhomogeneity of the sample. This feature was not reproduced in other samples.

The field H_{c1} is related to the vortex line energy ϵ_l through the thermodynamic relation $H_{c1} = 4\pi\epsilon_l/\Phi_0$. It is favorable for the vortex core to be at the CD since this decreases its energy. For $r \ll \xi$, a vortex gains the condensation energy $\pi r^2 H_c^2/8\pi$ when residing on CD [2, 99, 105]. The line energy ϵ_l^{cd} and the lower critical field H_{c1}^{cd} are then given by

$$\epsilon_l^{cd} = \epsilon_l^p - \left(\frac{\Phi_0}{4\pi\lambda}\right)^2 \left(\frac{r}{2\xi}\right)^2 \tag{7.1}$$

$$H_{c1}^{cd} = H_{c1}^p - \frac{\Phi_0}{4\pi\lambda^2}\left(\frac{r}{2\xi}\right)^2. \tag{7.2}$$

For the relative change in H_{c1} we obtain

$$\frac{\Delta H_{c1}}{H_{c1}^p} = \frac{H_{c1}^p - H_{c1}^{cd}}{H_{c1}^p} = \frac{(r/2\xi)^2}{\ln(\lambda/\xi)}. \tag{7.3}$$

For a temperature of 76 K, for example, using typical BSCCO parameters $\lambda = 1500/(1 - T/T_c)^{1/2}$ Å, $\xi = 40/(1 - T/T_c)^{1/2}$ Å and $r = 35$ Å for the radius of a CD, the relative change in H_{c1}, calculated by Eq. (7.30), is only $\sim 2\%$. One would expect that the corresponding relative reduction in

the penetration field would be of the same order of magnitude. In contrast, the measurements show that $\Delta H_p/H_p^p$, at 76 K, is $\sim 24\%$, much larger than $\Delta H_{c1}/H_{c1}^p$. In addition, the penetration of vortices into the irradiated regions is remarkably more abrupt than the penetration into the pristine region.

These observations raise the question - how such small differences in H_{c1} can cause such large variations in field penetration? As we show below, the sharp penetration of vortices into the irradiated regions with an overshoot to positive local magnetization, as well as the significant reduction in the penetration field, can be explained by a simple model describing the demagnetization effects in the pristine and the irradiated regions. We start by considering a long cylinder in a longitudinal field, where demagnetization effects are absent. We will continue with an ellipsoid in a perpendicular field where demagnetization effects are assumed to originate from the pristine matrix only. Then, we will generalize it to the case of an ellipsoid in a perpendicular field where demagnetization effects originate from both the pristine and irradiated regions.

Consider first a long cylinder in a longitudinal magnetic field H_a. In this geometry demagnetization effects are absent, and the internal magnetic field H coincides with H_a. In this ideal case the induction may be calculated precisely using the Ginzburg-Landau (GL) theory [106], and $B(H)$ exhibits infinite slope at $H_a = H_{c1}$ and tends to $B \approx H_a$ at $H_a \gg H_{c1}$. These characteristic features of $B(H)$ are reproduced by the simple model dependence

$$\begin{aligned} B(H) &= 0 \qquad\qquad\qquad \text{for} \quad H \le H_{c1} \\ B(H) &= (H^\alpha - H_{c1}^\alpha)^{1/\alpha} \quad \text{for} \quad H > H_{c1} \ , \end{aligned} \tag{7.4}$$

which closely fits the exact GL solution [106] for $\alpha \sim 2$–3 when $\kappa \gg 1$. Although $B(H)$ in the irradiated and pristine materials are in general different [100, 107], we shall show below that our main experimental findings can be

understood within the simplest approximation: the induction curves of the pristine and irradiated material exhibit the same $B(H)$ form that differs only by their lower critical field values H_{c1}^{p} and H_{c1}^{cd} in Eq. (7.4).

We now use these model $B(H)$ laws to calculate the inductions B^{p} and B^{cd}, in the pristine and in the irradiated regions, when H_a is perpendicular to the platelet. We shall consider our specimens as ellipsoids with some demagnetization factor N $(0 < N < 1)$, and assume first that the irradiated regions do not affect the overall demagnetization effects. This approximation is well justified if the relative volume c of the irradiated part of the sample is small. Then, the internal magnetic field $H = H_a - 4\pi N M(H)$ is obtained by solving the implicit equation

$$H + N(B^{p} - H) = H_a, \tag{7.5}$$

where $B^{p}(H)$ is the induction of the pristine material, and $M = (B^{p} - H)/4\pi$ is its magnetization. For an infinite platelet $(N = 1)$, Eq. (7.26) gives $B = H_a$ and the penetration field $H_{p}^{p} = 0$. For a finite platelet, the internal field H in the region $H_a < H_{p}^{p}$ is obtained from Eq. (7.26) by substituting $B^{p} = 0$. This yields

$$H \;=\; \frac{H_a}{1 - N} \quad \text{for} \;\; H_a \leq H_{p}^{p}. \tag{7.6}$$

The penetration fields for the irradiated and pristine regions are then given by

$$H_{p}^{p} \;=\; (1 - N) H_{c1}^{p} \tag{7.7}$$

$$H_{p}^{cd} \;=\; (1 - N) H_{c1}^{cd}, \tag{7.8}$$

respectively. For $H_a > H_{p}^{p}$, Eq. (7.26) can be solved numerically, but the sharpness of $B^{p}(H)$ in the vicinity of $H = H_{c1}^{p}$ means that $H \approx H_{c1}^{p}$ if

H_a does not exceed H_p too much. In this region of H_a (important for our experiments) Eq. (7.26) reduces to the form

$$B^p = \frac{H_a - H_p^p}{N} \quad \text{for} \quad H_a \geq H_p^p. \tag{7.9}$$

Note that in this approximation the H_a-dependence of B^p is *independent* of the explicit form of $B^p(H)$. The internal field H at $H_a \geq H_p^p$ is found by substituting the model $B^p(H)$ in the left hand side of Eq. (7.9). This yields

$$H = [(H_{c1}^p)^\alpha + (\frac{H_a - H_p^p}{N})^\alpha]^{1/\alpha} \quad \text{for} \quad H_a \geq H_p^p. \tag{7.10}$$

With this H, we get the induction $B^{cd}(H_a)$ in the irradiated regions:

$$B^{cd} = 0 \qquad \text{for} \quad H_a \leq H_p^{cd}, \tag{7.11}$$

$$B^{cd} = [(\frac{H_a}{1-N})^\alpha - (H_{c1}^{cd})^\alpha]^{1/\alpha} \qquad \text{for} \quad H_p^{cd} < H_a \leq H_p^p, \tag{7.12}$$

$$B^{cd} = [(H_{c1}^p)^\alpha + (\frac{H_a - H_p^p}{N})^\alpha - (H_{c1}^{cd})^\alpha]^{1/\alpha} \qquad \text{for} \quad H_a > H_p^p, \tag{7.13}$$

Expansion of Eqs. (7.12) and (7.13) around H_p^{cd} and H_p^p, respectively, shows that for $H_a \geq H_p^{cd}$, $B^{cd} \propto (H_a - H_p^{cd})^{1/\alpha}$, while for $H_a \geq H_p^p$, $B^{cd} \propto (H_a - H_p^p)^\alpha$. This means that $B^{cd}(H_a)$ sharply increases in the narrow interval $H_p^{cd} < H_a < H_p^p$, then it increases slowly. In contrast, $B^p(H_a)$, grows approximately linearly with H_a, as shown by Eq. (7.9).

The above calculation accounts for the sharp penetration of the magnetic field into the irradiated regions. However, it provides a good approximation only if the total volume of the irradiated regions is much smaller than the platelet volume. In addition, this approach does not explain how a small variation in H_{c1} results in a large variation in H_p. Note that according to Eqs. (7.7) and (7.8) the relative change in H_{c1} and in H_p should be the same. In

order to explain the measurements results and to allow the extraction of the lower critical fields, we now take into consideration the effect of the irradiated regions on the internal magnetic field H. Since this field is generated by a distribution of the magnetization over the whole sample, this effect can be approximately taken into account by a simple generalization of Eq. (7.26):

$$H + N\left[(1-c)(B^p - H) + c(B^{cd} - H)\right] = H_a, \tag{7.14}$$

where c is the relative volume of the irradiated part of the sample. The penetration field H_p^p is given by

$$H_p^p = (1-N)H_{c1}^p + cNB^{cd}(H_{c1}^p). \tag{7.15}$$

This equation immediately follows from Eq. (7.14), for $H_a = H_p^p$, $B^p = 0$, and $H = H_{c1}^p$. The penetration field H_p^{cd} is still defined by Eq. (7.8). The magnetic induction in the pristine region is approximately given by equations that is similar to Eq. (7.9), and that is valid unless $H_a \gg H_p^p$,

$$B^p = 0 \quad \text{for} \quad H_a \le H_p^p, \tag{7.16}$$

$$B^p = \frac{H_a - H_p^p}{N(1-c)} \quad \text{for} \quad H_a > H_p^p. \tag{7.17}$$

In the region $H_a \ge H_p^p$, H can be determined from Eqs. (7.17) and (7.4)

$$H = \left[(H_{c1}^p)^\alpha + \left(\frac{H_a - H_p^p}{N(1-c)}\right)^\alpha\right]^{1/\alpha} \quad \text{for} \quad H_a \ge H_p^p, \tag{7.18}$$

while in the interval $H_p^{cd} \le H_a \le H_p^p$ we use a linear interpolation of H between its values H_{c1}^{cd} and H_{c1}^p at the ends of this interval. Then, B^{cd} is approximately described by the equations

$$B^{cd} = 0 \quad \text{for} \quad H_a \le H_p^{cd}, \tag{7.19}$$

$$B^{cd} \approx B^{cd}(H_{c1}^p)\frac{H_a - H_p^{cd}}{H_p^p - H_p^{cd}} \quad \text{for} \quad H_p^{cd} < H_a \le H_p^p, \tag{7.20}$$

$$B^{cd} = [(H_{c1}^p)^\alpha + (\frac{H_a - H_p^p}{N(1-c)})^\alpha - (H_{c1}^{cd})^\alpha]^{1/\alpha} \quad \text{for } H_a > H_p^p, \tag{7.21}$$

that replace Eqs. (7.11)-(7.13). The inductions $B^p(H_a)$ and $B^{cd}(H_a)$ were also calculated exactly numerically by solving Eq. (7.14) for the internal field H and inserting this H into the models $B^p(H)$ and $B^{cd}(H)$. The approximate analytical expressions described above, agree with the numerical calculations very well in the relevant region of $H_a < 2H_p^p$.

The inclusion of the contribution from the irradiated regions, can noticeably increase H_p^p, As seen by comparing Eq. (7.15) and (7.7). As we now show, this explains how, in agreement with our measurements, small spatial variations in H_{c1} are amplified and lead to a large spatial variations in the penetration field. This amplification can be shown by defining $H_{c1}^{cd} = (1-\epsilon)H_{c1}^p$, where $0 < \epsilon \ll 1$, and writing the ratio between the relative changes in H_p and H_{c1} in terms of the sample parameters c, N and ϵ. From Eq. (7.15) and (7.8), with $\alpha = 3$, we obtain

$$\frac{\Delta H_{c1}}{H_{c1}^p} = \epsilon \tag{7.22}$$

$$\begin{aligned} \frac{\Delta H_p}{H_p^p} &= 1 - \frac{(1-N)(1-\epsilon)}{(1-N) + cN(1-(1-\epsilon)^3)^{1/3}} \\ &\approx \frac{3^{1/3}cN}{1-N}\epsilon^{1/3} + \epsilon \end{aligned} \tag{7.23}$$

and for the ratio we obtain

$$\frac{\Delta H_p/H_p^p}{\Delta H_{c1}/H_{c1}^p} \approx \frac{3^{1/3}cN}{1-N}\epsilon^{-2/3} + 1. \tag{7.24}$$

This ratio, which measures the amplification, is always larger than 1. Moreover, it increases and finally diverges as $\epsilon \to 0$. This means that the relative change in H_p is always larger than the relative change in H_{c1} and that this amplification becomes significantly larger as ΔH_{c1} vanishes. The amplification factor is 1 for $c \to 0$ and it grows linearly with c. For $N = 0$, where

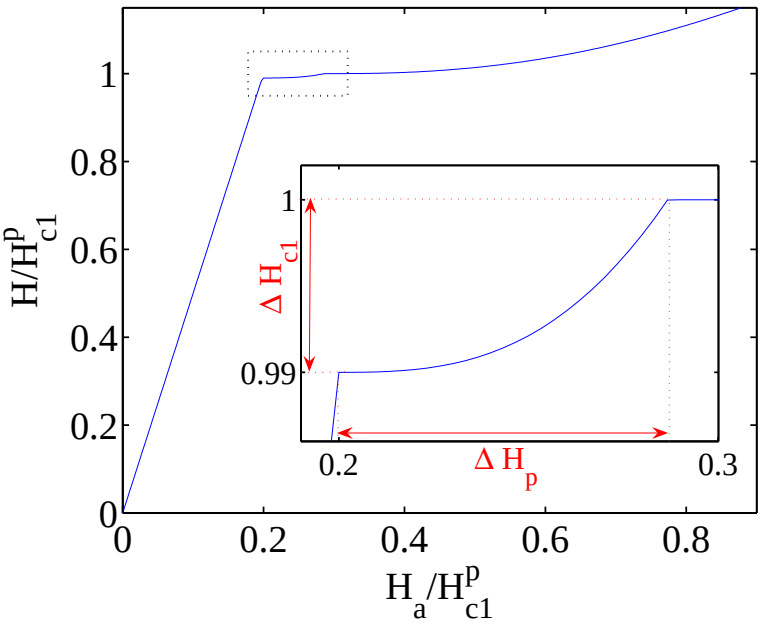

Fig. 7.9: The internal field H Vs. H_a. The inset shows a magnified view of the region $H_p^{cd} < H_a < H_p^p$ marked by the dotted rectangle.

demagnetization effects are absent, the amplification is also 1. This is inevitable since in this situation $H_p = H_{c1}$ in both the irradiated and pristine regions. Upon increasing N, the amplification diverges as $N \to 1$. We note that this amplification provides a tool to detect very small variations in H_{c1}.

To get a better understanding of this amplification we plot, in Fig. 7.9, the internal field H as a function of H_a. Initially, in the Meissner state, H increases linearly with a slope of $1/(1-N)$. This fast increase is suppressed at H_p^{cd} where vortices start penetrating into the irradiated regions. As shown by the magnified view of the region $H_p^{cd} < H_a < H_p^p$, above H_p^{cd}, H remains nearly constant and eventually starts increasing again. When H_a exceeds H_p^p, vortices start penetrating also into the pristine regions and the increase rate of H is suppressed once again. The vanishing slope dH/dH_a above H_p^{cd} leads

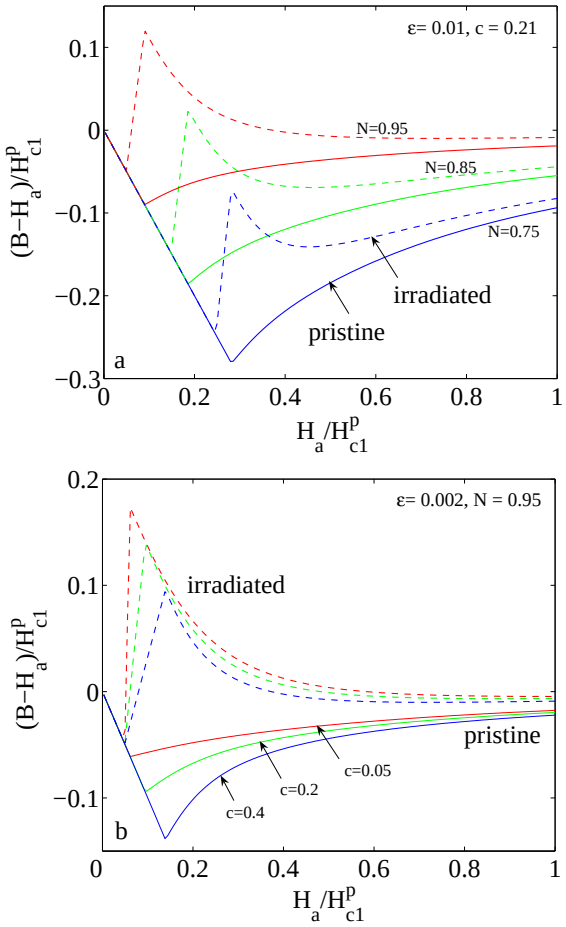

Fig. 7.10: Theoretical local magnetization curves in the pristine (solid) and irradiated (dashed) regions plotted in units of H_{c1}^{p}. (a) For $N = 0.75, 0.85$ and 0.95. (b) For $c = 0.05, 0.2$ and 0.4.

to the observed amplification. Note that above H_p^{cd}, in order to increase H by only a small amount, H_a should be increased significantly. Consequently, as demonstrated by the inset, a reduction of $\Delta H_{c1} = 0.01 H_{c1}^{p}$ in H_{c1} results in almost an order of magnitude increase in $\Delta H_p = 0.09 H_{c1}^{p}$ for $N = 0.8$ and $c = 0.35$.

The different effects of the sample geometry and the fraction of the irradiated area on the local magnetization are demonstrated in Fig. 7.10. The figure shows theoretical local magnetization curves $B - H_a$ for the pristine (solid) and irradiated (dashed) regions, plotted for different values of N and c. In Fig. 7.10a the curves are plotted for three values of N. The sharp penetration into the irradiated regions is clearly seen in Fig. 7.10a by the jump in the magnetization of the irradiated regions. Note that as N increases, H_p^p and H_p^{cd} shift downwards and the jump reaches higher values until, at $N = 0.85$, it starts overshooting towards positive values, similar to the measured curves displayed in Fig. 7.8b. In the opposite limit of $N \to 0$ the jump disappears and the magnetization curves of the irradiated and pristine regions show the same but shifted $B(H_a)$. In Fig. 7.10b we plot another set of theoretical curves, for different values of c. This figure clearly demonstrates the large effect of the irradiated regions on the penetration into the pristine regions. Upon increasing c from 0.05 to 0.4, H_p^p shifts to higher fields while H_p^{cd} remains unaffected. This upward shift in H_p^p is the amplification effect described by Eq. (7.24).

Figure 7.11 shows theoretical curves fitted to experimental data using the model $B(H)$ with exponent $\alpha = 2.4$. The solid lines are the measured local magnetization curves, obtained in crystal B, at 70 K, and the dashed lines are the theoretical fits. In the fit we used $c = 0.35$, the actual measured fraction of the irradiated regions, and $H_p^{cd} = 2.85$ Oe, as extracted from the experimental data. The best fit is obtained for $N = 0.825$ and $\epsilon = \Delta H_{c1}/H_{c1}^p = 0.04$. Apart from some deviations resulting due to inhomogeneities and the real shape of the sample, a very good agreement is observed, in particular near H_p^p and H_p^{cd}. This allows one to extract the thermodynamic lower critical fields. The present fit yields $H_{c1}^{cd} = 16.28$ Oe

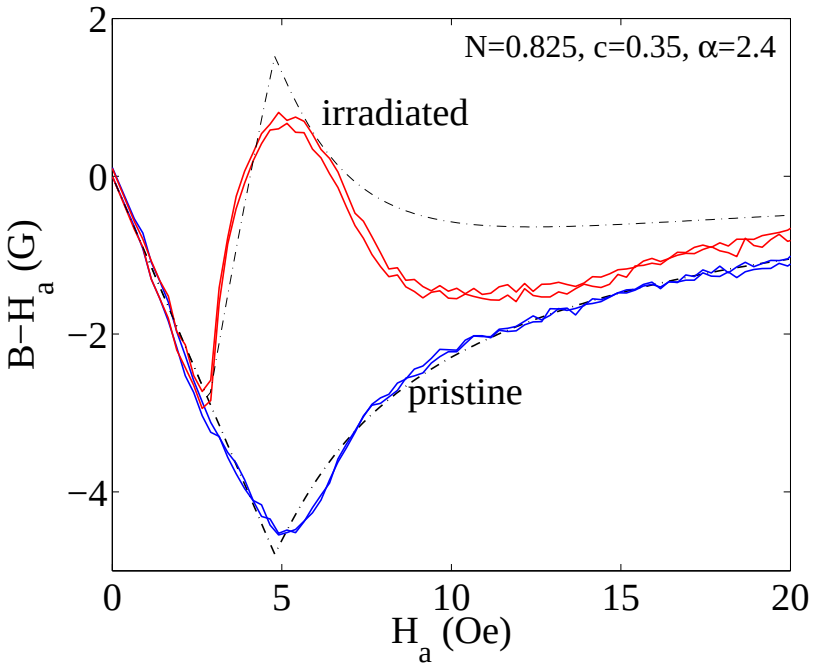

Fig. 7.11: Theoretical local (dashed dotted) magnetization curves for the pristine and the irradiated regions, fitted to experimental curves (solid) obtained in crystal B at 70K.

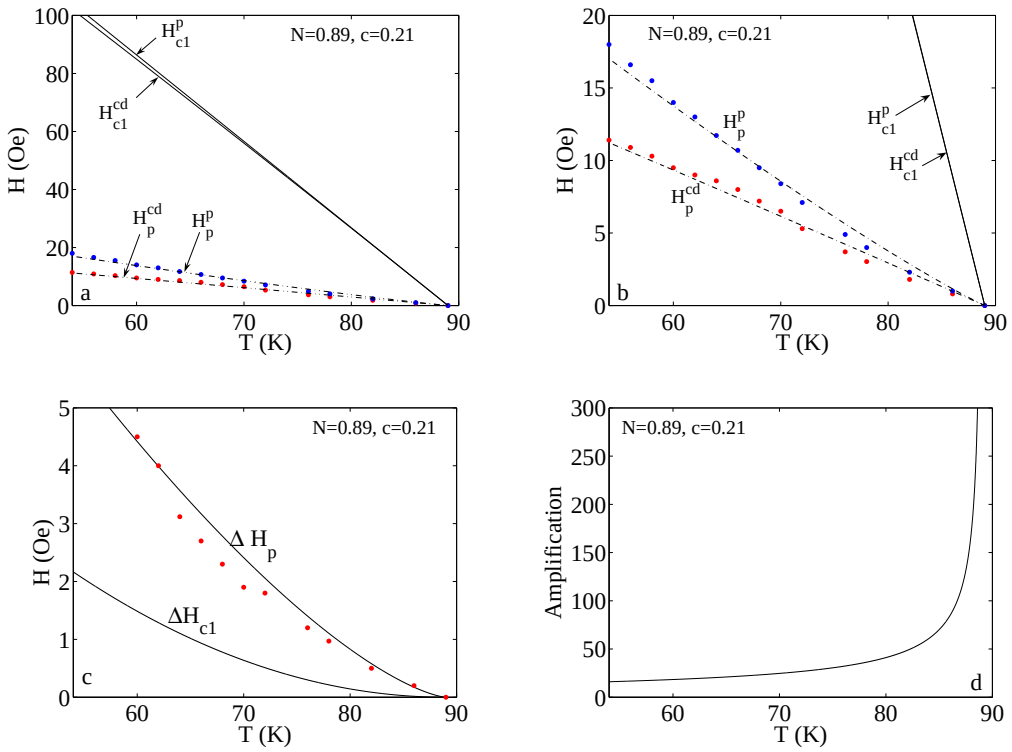

Fig. 7.12: (a) Theoretical (dashed dotted) and experimental (solid symbols) $H_p^p(T)$ and $H_p^{cd}(T)$ measured for sample A. The solid H_{c1}^p and H_{c1}^{cd} are the theoretical estimates used to calculate the theoretical $H_p^p(T)$ and $H_p^{cd}(T)$. (b) Magnified view of (a). (c) Theoretical (solid line) and experimental (solid symbols) $\Delta H_p(T)$ and ΔH_{c1} from (a). (d) The growth of the amplification factor Eq. (7.24) as ΔH_{c1} decreases.

and $H_{c1}^p = 16.95$ Oe. We note that the demagnetization factor resulting from the fit is in good agreement with our estimates of $N \sim 0.9$ obtained by approximating our samples as an ellipsoid with similar dimensions.

In Fig. 7.12a we plot the temperature dependence of $H_p^p(T)$ and $H_p^{cd}(T)$ for crystal A, in the temperature range above 55 K. Below this temperature no reversible magnetization could be attained in this crystal with our maximum H_{ac}, hence the equilibrium penetration fields could not be deter-

mined. The measured data is represented by the solid symbols and the calculated ones are shown by the dot-dashed lines. A very good fit is obtained. To calculate $H_p^p(T)$ and $H_p^{cd}(T)$ we first estimated the $H_{c1}^p(T)$ and $H_{c1}^{cd}(T)$ from the vortex line energy [Eq. (7.2)], using $\lambda = 1500/(1 - T/T_c)^{1/2}$ Å, $\xi = 40/(1-T/T_c)^{1/2}$ Å and $r = 35$ Å . Then we used our model [Eq. (7.15), (7.8)], with $\alpha = 2.4$ and $c = 0.21$, the relative irradiated volume in sample A, to calculate $H_p^p(T)$ and $H_p^{cd}(T)$. The best fit is obtained for $N = 0.89$. Figure 7.12b shows a magnified view of the fit between the theoretical and the experimental $H_p^p(T)$ and $H_p^{cd}(T)$. In Fig. 7.12c we plot the calculated $\Delta H_{c1}(T)$ and the correspondence of the theoretical and measured $\Delta H_p(T)$. Note that at high temperatures $\Delta H_{c1}(T)$ becomes very small and above 85 K drops below 30 mOe, which would be below our experimental resolution. Yet, due to the amplification, $\Delta H_p \sim 300$ mOe, is still large enough to be detected. It turns out that such a geometry with strong demagnetization effects enables to detect small variations in H_{c1} down to about a few mOe, which could not have been detected in the ideal longitudinal geometry. In Fig. 7.12d we plot the amplification factor as a function of temperature. Since ϵ, the relative change in H_{c1}, decreases with temperature due to the temperature dependence of λ and ξ, this figure demonstrates the increase of the amplification as ΔH_{c1} decreases, by factors of more than 100.

In summary, we used magneto optical measurements combined with the shaking technique to study the equilibrium field penetration into superconducting thin platelets containing small regions in which CDs were introduced by heavy ion irradiation. We observed reduction of H_{c1} due to CDs and a remarkably abrupt field penetration into the irradiated regions. We derived a model that shows how geometrical effects can enhance small differences in the lower critical field and lead to large variations in the local penetration

field. These phenomena should be very important in inhomogeneous samples - a minute material inhomogeneities can significantly affect the way the field penetrates into the sample and can result in large variations in the local induction.

7.3 Local magnetization measurements in Mn_{12} crystals

Molecular magnets, or single molecule magnets, are typically composed of magnetic cores surrounded by organic complexes. With a total spin of $S = 10$ and strong easy axis anisotropy [52, 108, 109, 110, 111, 112, 113, 114], $[Mn_{12}O_{12}(CH_3COO)_{16}(H_2O)_4] \cdot 2CH_3COOH \cdot 4H_2O$ (generally referred to as Mn_{12}-acetate) has received a great deal of attention. When crystallized, Mn_{12} forms a tetragonal lattice [115] with the easy magnetization direction along the c-axis. The magnetic cores are well separated [115], so that exchange interactions between the molecules are negligible [111, 112, 113, 116]. The main terms in the spin Hamiltonian of Mn_{12} are given by

$$H = -DS_z^2 - g_z\mu_B B_z S_z - AS_z^4$$

The first term is the magnetic anisotropy energy, with $D = 0.548(3)$K while the third term represents the next higher-order term in longitudinal anisotropy, with $A = 1.173(4) \times 10^{-3}$K [117, 118, 119]. The second term is the Zeeman coupling to a magnetic field B_z along the easy-axis. In the absence of a magnetic field, this Hamiltonian can be represented as a symmetric double well potential with a set of energy levels corresponding to the $(2S + 1) = 21$ allowed values of the quantum number S_z. A magnetic field B_z lifts the degeneracy of $\pm S_z$ states on opposite sides of the potential barrier, and a strong field B_z causes most of the molecules to occupy states in one of the wells. When B_z is swept, e.g., from positive to negative values, molecules relax from one side of the potential barrier to the other either via thermal activation over the barrier or by quantum tunneling through the barrier. Measurements below the blocking temperature of 3K show resonant tunneling of the magnetization, manifested as a series of steep steps in the hysteresis loop at roughly equal intervals of magnetic field [120, 3, 121, 51].

The steps occur at magnetic field values where states on opposite sides of the barrier have the same energy, and are at "resonance".

One of the common experimental techniques to study the tunneling of the magnetization is to measure the magnetic response of the crystal when an external magnetic field H_a is applied parallel to the easy axis, and is swept through a series of resonances along the hysteresis loop. To date, studies of extended samples have provided the magnetic induction (and its variation in a swept magnetic field) as averages over the whole sample, or they have assumed that values measured in a limited region of space represent the average. As such, these measurements do not provide any information on the spatial profile of the magnetization in the sample, or on how the relaxation process propagates spatially within the sample.

The experiment reported here utilizes an array of sensors to measure the spatial variation of the magnetization in a Mn_{12} crystal as H_a is swept. Within our model we find the magnetization to be significantly non-uniform along the sample, with the non-uniformity being enhanced within the steps. Furthermore, it appears that different regions of the sample are at resonance at different values of the applied field, and that the sweep rate of the internal magnetic induction is spatially non-uniform. We demonstrate that the degree of non-uniformity can be manipulated by sweeping the magnetic field back and forth through part of the resonance.

The local induction of single Mn_{12} crystals of typical size $400 \times 100 \times 40$ μm^3 was measured using an array of eleven Hall sensors [29]. The active layer of these sensors is a two dimensional electron gas formed at the interface of GaAs/AlGaAs heterostructure. The samples were mounted onto the surface of an array of 10×10 μm^2 sensors that were 10 μm apart, with the easy-axis parallel to the z-direction and to the applied field H_a, as shown in Fig. 7.13.

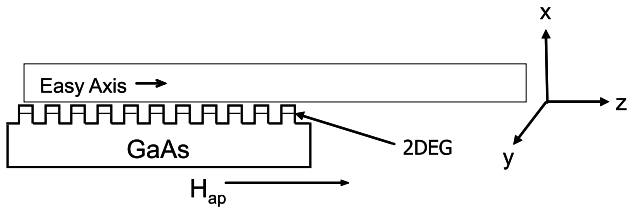

Fig. 7.13: Schematic diagram of the experimental setup. The Mn_{12} crystal, with a typical size of $z = 400\ \mu m$, $y = 100\ \mu m$ and $x = 40\ \mu m$ is placed directly on the surface of an array of $10 \times 10\ \mu m^2$ sensors that are $10\ \mu m$ apart. The sensors cover only half the sample and measure the perpendicular component (B_x) of the magnetic induction at the surface.

The eleven sensors measure B_x, the x-component of the magnetic induction due to the magnetization of the crystal. Since the two dimensional electron gas resides only 0.1 μm below the surface, the induction measured by the sensors is practically equal to the induction at the crystal surface. As shown in Fig. 7.13, the center of the crystal was aligned with the array so that ten sensors probed the field along half the crystal length and the last sensor measured the field at the edge of the sample.

Fig. 7.14a and 7.14b show two local hysteresis loops of $B_x(H_a)$, at $T = 0.3K$, measured simultaneously at the edge of the sample and close to its center. The curves were obtained starting from a fully magnetized state by sweeping H_a from -6T up to 6T and back. The loop measured locally at the edge of the sample (Fig. 7.14a) resembles previously measured magnetization loops. When increasing H_a from zero to 6T, B_x increases monotonically toward its positive saturation value while displaying a series of steep steps at roughly equal intervals of magnetic field, due to resonant tunneling of the magnetization.

In contrast, the magnetic induction measured close to the center of the sample (shown in Fig. 7.14b) displays non-monotonic behavior as a function

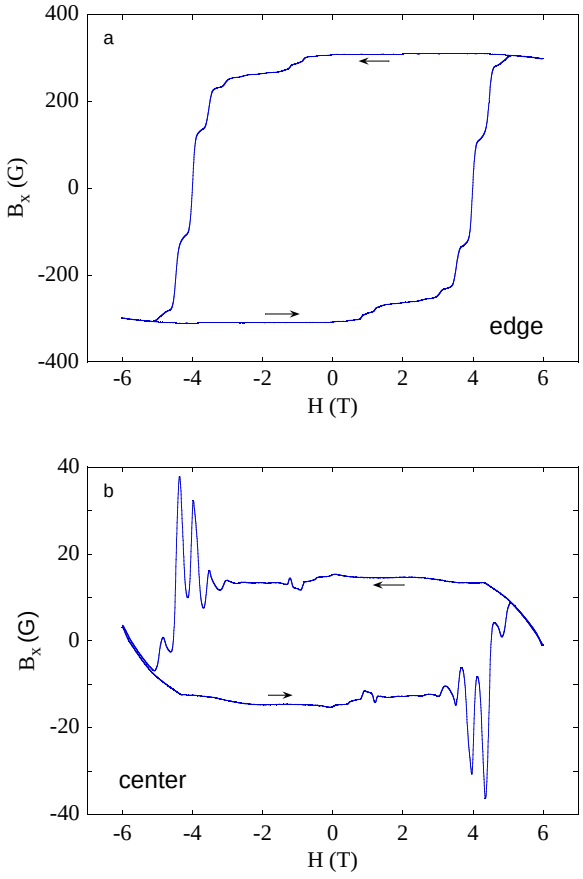

Fig. 7.14: Local hysteresis loops of B_x as a function of H_a ($T = 0.3$K) , measured simultaneously at two different positions on the sample: (a) close to the edge and, (b) close to the center of the sample.

of H_a. The resonances are not manifested by a series of steps, but rather by a series of peaks and dips whose width is larger than that of the steps in Fig. 7.14a. Similar behavior is observed at other sensors located between the edge and the center of the sample. In general, B_x is largest close to the edge and decreases towards the center of the sample. The non-monotonic dependence on H_a, however, is most pronounced close to the center and gradually diminishes when proceeding towards the edge of the sample. The

remarkable difference in the dependence of B_x on H_a observed by the different sensors contradict the assumption that the magnetization is uniform inside the sample. In general [122], $B_x(\vec{r}, H_a) = \int d\vec{r'} M(\vec{r'}, H_a) f(\vec{r} - \vec{r'})$, where $M(\vec{r'}, H_a)$ is the magnetization at point $\vec{r'}$, that is assumed to be parallel to the easy axis, and

$$f(\vec{r} - \vec{r'}) = -\frac{3(z - z')(x - x')}{|r - r'|^5}$$

If $M = M_0(H_a)$ is independent of $\vec{r'}$, we get $B_x(\vec{r}, H_a) = M_0(H_a) \int d\vec{r'} f(\vec{r} - \vec{r'})$, so that the $B_x(H_a)$ curves measured by all sensors should collapse onto a single curve when multiplied by a scaling factor. As the inner curves are non-monotonic while the edge curves are monotonic, this scaling cannot be realized, and the magnetization is therefore non-uniform.

The non-uniformity of the magnetization is the source of the non-monotonicity displayed in Fig. 7.14b. Spins pointing in the same direction that are located on opposite sides of a sensor make *opposite* contributions to B_x. Due to these opposite contributions, the magnetic induction B_x measured by a sensor located close to the center of the sample is very small when all the spins in its surrounding point in the same direction, but is enhanced when the magnetization on the two sides is different. This enhancement may bring B_x to a value larger than its value when the sample becomes fully magnetized, as shown in Fig. 7.14b. Now, if the relaxation rates on the two sides of the sensor are different, the non-uniformity in the magnetization varies, and so does B_x. The direction in which B_x varies with H_a indicates the relative magnitudes of the relaxation rates on the two sides of the sensor. The situation is different for a sensor located near the edge of the sample, where all spins are on one side, and therefore their contributions to B_x add. For this sensor, inhomogeneities in the magnetization only broaden the steps, but do not result in non-monotonic behavior. This qualitative picture is further

discussed below in terms of an equation for the time evolution of the local magnetization.

We now proceed to extract the spatial profile of the magnetization from the profile $B_x(z)$ measured by the sensors. Assuming that the sample has a perfect rectangular shape, and the magnetization is uniform along the x and y directions, the induction B_x can be written as

$$B_x(z) = -\int dz' F(z-z') \frac{\partial M(z')}{\partial z} \tag{7.25}$$

where

$$F(z-z') = \log \frac{w_1 + \sqrt{w_1^2 + d_1^2 + (z-z')^2}}{w_1 + \sqrt{w_1^2 + d_2^2 + (z-z')^2}} - \log \frac{w_2 + \sqrt{w_2^2 + d_1^2 + (z-z')^2}}{w_2 + \sqrt{w_2^2 + d_2^2 + (z-z')^2}} \tag{7.26}$$

For the samples we used, $d_1 = 0.1\ \mu m$ is the distance in the x direction between the sample surface and the 2DEG, $d_2 = 40\ \mu m$ is the distance between the 2DEG and the sample's other surface, and $w_1 = -5\ \mu m$, $w_2 = 85\ \mu m$ are the distances between the center of the sensors and the edges of the sample in the y-direction.

$F(z-z')$ is a short-range function, whose characteristic decay length is typically 10 μm for our geometry. Eq. (7.25) implies that the magnetic field B_x measured by a sensor on the sample surface is proportional to the derivative $\frac{\partial M}{\partial z}$ in the vicinity of the sensor, and therefore Figs. 7.14a and 7.14b approximate the dependence of $\frac{\partial M}{\partial z}$ on H_a at the edge of the sample and close to the center of the sample, respectively.

Assuming that the magnetization varies smoothly over the scale of our sensors, we interpolate the measured $B_x(z)$ and numerically invert the kernel $F(z-z')$ to extract the magnetization profile $M(z, H_a)$. Figure 7.15 shows the resulting magnetization as a function of position for various values of H_a.

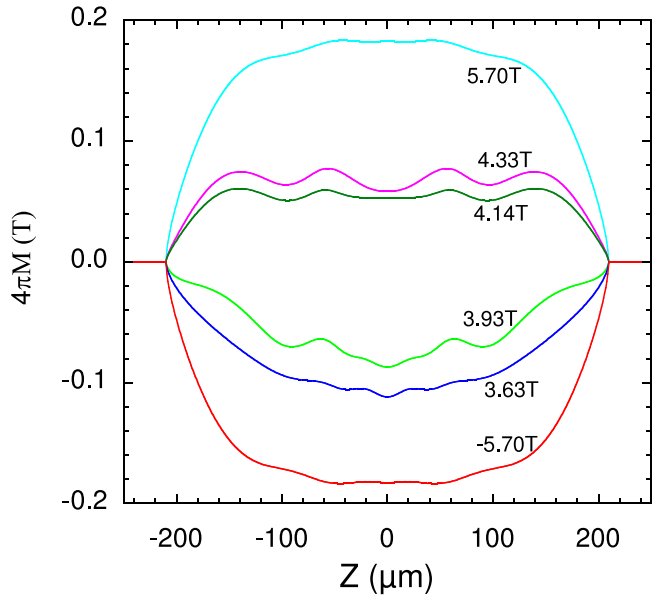

[!]

Fig. 7.15: The calculated profile of the magnetization plotted as a function of the distance from the center of the sample, at six different values of the applied field. Note the enhanced non-uniformity at fields close to resonances, at 3.9T and 4.33T.

Since our sensors cover only half the sample, we rely on the (nearly) symmetric shape of the samples and assume the magnetization to be symmetric with respect to the sample center. The non-uniformity of the magnetization and its evolution as a function of H_a are clearly demonstrated. Focusing first on the central part of the sample, we note that at -5.7T, where the sample is presumably fully magnetized, the magnetization is approximately uniform. When increasing the field to 3.6T the magnetization starts to develop a small amount of non-uniformity, manifested by the small variations of the magnetization from the average value. These variations continue to develop and become more pronounced at 3.9T, when the magnetization in most of the sample shows a high relaxation rate. The non-uniformities then decay somewhat at 4.14T, where the sample is out of resonance, and become prominent once more at the next resonance, at 4.3T. When increasing the field further to 5.7T the non-uniformities disappear and the magnetization becomes uniform again. Non-uniformities similar to those presented in Fig. 7.15 were observed in several samples, where they are enhanced when most of the sample is at resonance, and become minor away from resonances.

At the very edge of the sample the magnetization is expected to change abruptly from zero outside the sample to a non-zero value inside the sample. We believe that the gradual variation observed at all field values results from two major sources. First, the field B_x at the edge of the sample varies significantly over the length of one sensor, and therefore the average field measured by the edge sensor may deviate appreciably from its local value. Second, the calculation of the magnetization is carried out assuming the sample has a perfect rectangular shape. Deviations from this shape, for example edges that are not perpendicular to the plane of the sensors, could also contribute to the rounding of the data at the edges. Note, however, that

these effects cannot introduce the observed non-uniformities in the center of the sample. We also note that the overall scale of the magnetization obtained from our calculation is not very different from that expected: at full magnetization, $4\pi M$ is 0.12T for Mn_{12} crystals, while the maximum value shown in Fig. 7.15 is 0.18T.

The non-uniformity of the magnetization implies that B_z, the internal magnetic field in the z direction, is spatially non-uniform. Consequently, different parts of the sample enter the resonance at different values of H_a. We will now demonstrate that the internal sweep rate $\frac{\partial B_z}{\partial t}$ is spatially non-uniform as well, so that different parts of the sample spend different times at resonance. Under the assumption used to extract $M(z)$, B_z inside the sample can be written as

$$B_z(z) = H_a + 4\pi M(z) + \int dr' \frac{\partial M(r')}{\partial z'} \frac{z - z'}{|r - r'|^3} \tag{7.27}$$

Since all the terms and their time dependence are available from our analysis, we can directly derive the local sweep rate $\frac{\partial B_z}{\partial t}$.

This is shown in Fig. 7.16 as a function of position in the central part of the sample for different values of H_a. Two major observations are of particular interest. The first is that at 3.9T and at 4.3T, when the sample is at resonance, the internal sweep rate is much higher than the nominal sweep rate of the external field. For example, $\frac{\partial B_z}{\partial t}$ is about 2.5 times larger than $\frac{\partial H_a}{\partial t}$ at 3.9T. In contrast, at 3.6T and 4.1T, when the sample is out of resonance, the sweep rates of B_z and H_a are approximately equal. The second major observation is that at resonance fields, $\frac{\partial B_z}{\partial t}$ is highly non-uniform and can vary by as much as 20% over a distance of the order of 50 μm. This means not only that different regions enter the resonance at different H_a, but also that the times spent by local regions at resonance can be significantly different.

As we show below, the observed spatial non-uniformities and their evolu-

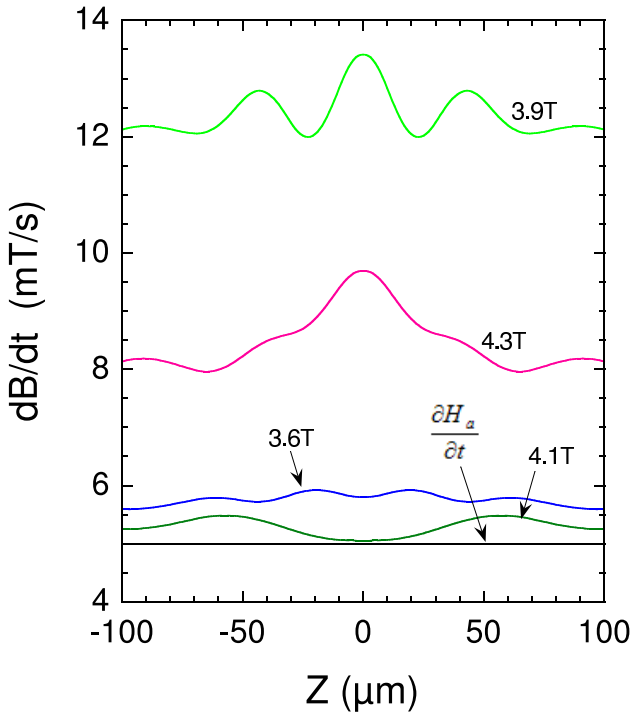

Fig. 7.16: Calculated sweep rate of the internal field, $\frac{\partial B_z}{\partial t}$, plotted as a function of the distance from the center of the sample, for the same field values as in Fig. 7.15. Note that when most of the sample is at resonance, at 3.9T and 4.3T, the internal sweep rate $\frac{\partial B_z}{\partial t}$ is much higher than the external sweep rate, $\frac{\partial H_a}{\partial t}$. Moreover, at these fields $\frac{\partial B_z}{\partial t}$ is significantly non-uniform inside the sample. When the sample is out of resonance, at 3.6T and 4.1T, the internal sweep rate is approximately uniform inside the sample and is very close to the sweep rate of the external field.

tion with H_a can be explained by a simple model describing the relaxation of the magnetization along the hysteresis loop. Initially, at 6T, the magnetization is uniform inside the sample. However the relaxation rate is non-uniform due to the spatial variation of the internal magnetic field and due to molecular and structural disorder. Therefore, as we sweep the magnetic field to -6T (in the opposite direction) non-uniformity in the magnetization begins to develop. Under certain conditions, and particularly within resonances, the non-uniformity in the magnetization grows with time, despite the decay in the magnetization itself. The magnetization is non-uniform even when the sample is out of resonance and the relaxation rates are negligible. We attribute the non-uniformity in the magnetization off resonance to the spatial variation of the sweep rate (Fig. 7.16) that causes different regions of the sample to spend different times at resonance.

In our model the relaxation of the space- and time-dependent magnetization $M(z,t)$ is governed by the equation

$$\frac{\partial M}{\partial t} = -(M - M_0)\Gamma \tag{7.28}$$

where M_0 is the equilibrium magnetization and Γ is the relaxation rate, which near a resonance has a general form

$$\Gamma = \Gamma_0 \frac{\alpha^2}{(B_z - B_r)^2 + \alpha^2} \tag{7.29}$$

where B_r is the magnetic induction at the center of the resonance, and 2α is the resonance width. Molecular disorder introduces variations of Γ_0, B_r and α between different molecules. However, since the distribution of these parameters does not depend on position, we use their average values. The non-uniformity of the magnetization is characterized by its spatial derivative $\frac{\partial M}{\partial z}$. We may use Eq. (7.28) to analyze the time evolution of $\frac{\partial M}{\partial z}$. To that end, we take the derivative of (4) with respect to z, and approximate

$B(z) \approx H_a + 4\pi M(z)$(i.e., we neglect the third term in Eq. (7.27), which is small in the central part of the sample). We obtain

$$\frac{\partial}{\partial t}\frac{\partial M}{\partial z} = -[\Gamma + 4\pi(M - M_0)\frac{\partial \Gamma}{\partial B}]\frac{\partial M}{\partial z} \tag{7.30}$$

Although the dependence of Γ on $M(z)$ makes this equation a non-linear differential equation, the conditions under which non-uniformities in the magnetization grow with time are rather transparent. The question of whether the magnitude of $\frac{\partial M}{\partial z}$ increases or decreases with time is determined by the balance between the two terms on the right hand side of this equation. The first term acts to suppress the magnitude of $\frac{\partial M}{\partial z}$, i.e., the magnitude of the non-uniformity. The effect of the second term, on the other hand, depends on the sign of $(M - M_0)\frac{\partial \Gamma}{\partial B}$. When this sign is negative, this term tends to enhance the magnitude of the non-uniformity. If strong enough, it may overcome the effect of the first term. When that happens, the magnetization $M(z)$ relaxes towards M_0, but its non-uniformity $|\frac{\partial M}{\partial z}|$ increases with time.

From Eq. (7.30), it is easy to verify that as long as $|M - M_0| < \frac{\alpha}{4\pi}$,

$$\Gamma + 4\pi(M - M_0)\frac{\partial \Gamma}{\partial B} > 0 \tag{7.31}$$

for any B_z and hence the non-uniformity is suppressed with time. However, when $|M - M_0| > \frac{\alpha}{4\pi}$, there is a range of B_z

$$(M - M_0) - \sqrt{(M - M_0)^2 - \frac{\alpha^2}{(4\pi)^2}} < \frac{(B_z - B_r)}{4\pi} < (M - M_0) + \sqrt{(M - M_0)^2 - \frac{\alpha^2}{(4\pi)^2}} \tag{7.32}$$

at which $\Gamma + 4\pi(M - M_0)\frac{\partial \Gamma}{\partial B} < 0$ and the non-uniformity is enhanced with time. We consider, for concreteness, the case where H_a is swept down from 6T to -6T through one of the resonances. In this case M_0 is negative, and

$M - M_0$ is positive. If $M - M_0 >> \frac{\alpha}{4\pi}$, the range (7.32) occupies the first half of the resonance, where $B_z > B_r$. As H_a is swept down, the non-uniformity grows during the first half of the resonance while $B_z > B_r$, and then is suppressed again when B_z drops below B_r. Such behavior is indeed observed in Fig. 7.15. In general, non-uniformities are always enhanced on approaching resonance, reaching maximum close to resonance and then suppressed after the resonance. Our measurements show resonances whose half-widths are about 0.045T. However, the measured half-widths are larger than the intrinsic half-width α, due to the effects of molecular disorder and hyperfine fields. The non-uniformities are found experimentally to evolve at the resonances where $4\pi(M-M_0) > 0.06$T, consistent with the model above.

Eq. (7.29) and the discussion following it suggest that the non-uniformity in the magnetization may be enhanced if the applied field H_a is tuned to a value where $\Gamma + 4\pi(M - M_0)\frac{\partial \Gamma}{\partial B}$ is negative at least in some parts of the sample, and is kept there for some time [123]. Our measurements show that this is indeed the case. To identify the proper value of H_a, we note again that B_x is proportional to $\frac{\partial M}{\partial z}$ and therefore the observed slope $\frac{\partial B_x}{\partial H_a}$ measures the local slope $\frac{\partial}{\partial z}\frac{\partial M}{\partial t}$. Thus, when H_a is swept back and forth over a region where both $\frac{\partial B_x}{\partial H_a}$ and B_x have the proper signs, this sweep results in an enhancement of the non-uniformity. Figure 7.17a shows the effect of such a back-and-forth sweep on the magnetic induction B_x measured by a sensor located close to the center of the sample. Two curves are presented: a reference curve in which H_a was swept between -6T and 6T at a constant sweep rate; and the 'back-and-forth sweep' (BF sweep) curve in which H_a was swept up from -6T to 3.9T and then was swept back and forth between 3.9T and 3.69T. The reference curve shows a dip at 3.9T, signifying resonant relaxation of the magnetization. The range of the back-and-forth sweep

was chosen to cover only half of this dip, at which both $\frac{\partial B_x}{\partial H_a}$ and B_x were negative. During the back-and-forth sweep the magnetic induction $|B_x|$ at $H_a = 3.9$T increased to a value 3.5 times larger than its corresponding value at the reference curve. The strong increase in $|B_x|$ above the saturation value signifies a strong enhancement of the non-uniformity inside the sample, since B_x is proportional to the local spatial derivative of the magnetization, $\frac{\partial M}{\partial z}$, in the vicinity of the sensor.

Figure 7.17b demonstrates the enhancement of the non-uniformity in the magnetization profile $M(z)$ by the BF sweep. The lowest curve shows the magnetization at 3.68T just before sweeping the field back and forth over part of the resonance. At this point some non-uniformity has already developed. The three other curves correspond to three different measurements in which BF sweeping was carried out with three different amplitudes. In all measurements the cycle starts at the same field of 3.7T, and each measurement spans a different part of the transition. The most significant enhancement of the non-uniformity is displayed for the smallest amplitude of 0.08T, where the number of molecules that relaxed during the BF sweep strongly differs between the center and the edge of the sample. The effect is smaller for an amplitude of 0.14T, and yet smaller for an amplitude of 0.25T. While suggesting the possibility for magnetization non-uniformities that grow with time, Eqs. (7.29) and (7.30) also indicate that eventually, as relaxation progresses and the magnitude of $M - M_0$ gets smaller, $\Gamma + 4\pi(M - M_0)\frac{\partial \Gamma}{\partial B}$ must at some point become positive. Since $\frac{\partial M}{\partial z}$ is approximately proportional to the magnetic induction B_x measured by our sensors, this implies that when H_a is swept back and forth for long enough, the magnitude of B_x must eventually decrease. This expectation is indeed borne out in the measurement. The inset of Fig. 7.17a presents the evolution of B_x during the back-and-

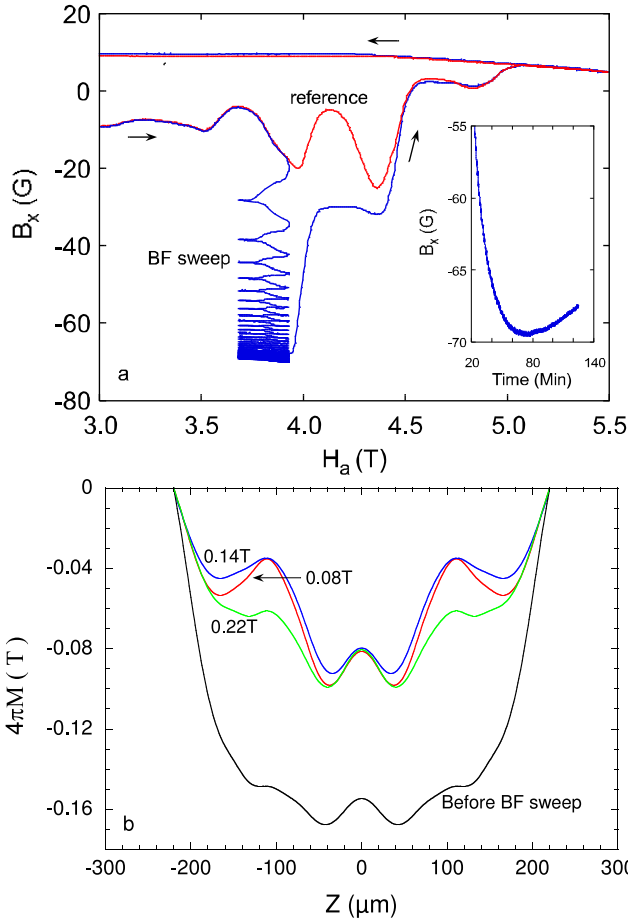

Fig. 7.17: Local hysteresis loops $B_x(H_a)$, measured close to the center of the sample. During the back and forth sweep the magnetic field B_x at $H_a = 3.9$T decreases to -70G, which is 3.5 times larger than its corresponding value at the reference curve (-20G). The inset shows the evolution of B_x as a function of time during the BF sweep. (b) Magnetization profiles $M(z)$ showing the enhancement of the non-uniformity by the BF sweep. The lowest curve shows the magnetization at 3.68T before the BF sweep. The upper curves correspond to three different measurements in which the BF sweep was carried out with different amplitude of the BF cycle (0.08T, 0.14T, 0.22T)

forth sweeping as a function of time. The measured B_x initially increases in magnitude, but after about 70 minutes of sweeping, its magnitude starts to decrease. This change happens when the difference between the relaxation rates on both sides of the sensor changes sign. The source of this change in relaxation rates may be the decrease of the magnitude of $M-M_0$, or a change in the internal magnetic induction B_z that changes both Γ and $\frac{\partial\Gamma}{\partial B}$. We are presently unable to determine the relative weight of these two sources.

The saturation of the non-uniformity when $M - M_0$ becomes too small is plausibly also the source of the effect of the BF sweep on the following resonance. As shown in Fig. 7.17a, the BF sweeping of the field in the range between 3.69T and 3.9T changes the dip seen in the reference curve at 4.3T into a step. Within the framework of Eq. (7.29), the non-monotonic behavior of B_x around 4.3T, shown in the reference curve, signifies an enhancement of the non-uniformity followed by its suppression. In contrast, the almost monotonic step observed in the BF curve indicates that as a consequence of the back-and-forth sweep, the resonance at 4.3T is traversed with $\Gamma+4\pi(M-M_0)\frac{\partial\Gamma}{\partial B}$ remaining positive, such that no enhancement of the non-uniformity takes place.

To summarize, we used a set of Hall sensors to measure the local magnetic response of crystals of the molecular magnet Mn_{12}-acetate. Our measurements allowed us to determine the local magnetization in different regions of the crystal and its evolution as the crystal is driven through a hysteresis loop. We find significant non-uniformities, which are larger when resonant tunnelling takes place, but do not disappear when out of resonance. We explain how these non-uniformities result from the dipolar interaction between molecules. We show that the non-uniformity of the magnetization may be enhanced by sweeping the externally applied field back and forth through a

properly chosen range. This method carries the potential for local manipulation of the magnetization profile inside the sample.

8. SUMMARY

The main goal of the work on High-T_c superconductor was to study the dynamic and thermodynamic behavior of the vortex matter in the presence of disorder. For this purpose we produced $Bi_2Sr_2CaCu_2O_8$ crystals with localized regions of correlated disorder. The correlated disorder was created by irradiation of the crystal with heavy ions. The defects were produced only in specific regions. This enables a sensitive comparison between irradiated and non-irradiated regions located in proximity. The comparison between neighboring regions avoids possible differences arising from intrinsic inhomogeneities of the sample. The samples were measured using conventional magneto-optics and differential magneto-optics with different kinds of modulations. The mode of modulation was chosen according to the transition or phenomena that we aimed to detect.

First we addressed the issue of dynamic vs. thermodynamic properties of the vortex matter in the presence of columnar defects. We investigated the influence of the angle between the applied field and the CDs on the dynamic and thermodynamic properties of the porous vortex matter. Our results were unexpected − we found that the dynamic properties are significantly affected by tilting the field away from the columnar defects, while the thermodynamic properties remained unaffected. This apparent discrepancy was resolved in this work using numerical simulations which have shown that when tilting the field away from the columnar defects, the vortices adopt a staircase shape

which preserves the thermodynamics but affects the dynamics significantly.

In further measurements we used magneto-optical measurements combined with the shaking technique to investigate the equilibrium behavior of the vortex matter near the lower critical field H_{c1}, which separates the Meissner state from the mixed state. A direct determination of H_{c1} is difficult due to non-equilibrium conditions which arise due to energy barriers against vortex penetration. Using the shaking method, however, we were able to suppress the irreversibility and study the way the field penetrates into superconductors. We showed that small local variations in the lower critical field dramatically affect the way the field penetrates into superconductors. We derived a theoretical model which explains how the influence of small sample inhomogeneities is enhanced by geometrical effects and leads to significant variations in the local field distribution and penetration. These phenomena should be very important in inhomogeneous samples - a minute material inhomogeneities can significantly affect the way the field penetrates into the sample and can result in large variations in the local induction.

The main goal of the study of Mn_{12} was to utilizing the local-Hall sensors technique, which was used in our lab in the study of high-T_c superconductors, in order to study the spatial behavior of the magnetization in single molecule magnets.

The material of choice was Mn_{12}-acetate. The samples were placed on an array of Hall sensors and the magnetic response was measured at several locations along the sample. This enabled us to extract the profile of the magnetization along the sample and to investigate the way this profile evolves upon sweeping the external field through the resonances.

We found that the magnetization is significantly non-uniform along the sample and that this non-uniformity is enhanced within the resonance steps.

Non-uniformity in the magnetization implies that the internal field B_z is not uniform inside the sample and therefore the resonance does not occur uniformly throughout the sample. This phenomenon was demonstrated very clearly in our measurements. Using the local measurements we could also calculate the spatial profile of the internal field $B_z(x)$, and its time derivative $dB_z/dt(x)$. We have shown that not only $B_z(x)$ but also $dB_z/dt(x)$ is not uniform inside the sample. This means that different parts of the sample spend different time in resonance.

We derived a theoretical model that describes the relaxation of the magnetization along the hysteresis loop and explains how, under certain conditions, the dipolar interaction between molecules enhances the non-uniformity in the magnetization during resonant relaxation. In further measurements we have shown that indeed, by sweeping the externally applied field back and forth through a properly chosen range within the resonance, we were able to enhance the non-uniformity in the magnetization. This method carries the potential for local manipulation of the magnetization profile inside the sample. We note that these observations should be taken into consideration when trying to glean quantitative information regarding the tunneling mechanism, like tunnel splitting and resonance width, from magnetization measurements.

9. LIST OF PUBLICATIONS

1. **'Inverse' melting of a vortex lattice**

   Nurit Avraham, B. Khaykovich, Y. Myasoedov, M. Rappaport, H. Shtrikman, D. E. Feldman, T. Tamegai, P. H. Kes, Ming Li, M. Konczykowski, C. J. van der Beek and E. Zeldov

   Nature 411, 451 (2001).

2. **First-order disorder-driven transition and inverse melting of the vortex lattice**

   Nurit Avraham, B. Khaykovich, Y. Myasoedov, M. Rappaport, H. Shtrikman, D. E. Feldman, E. Zeldov, T. Tamegai, P. H. Kes, Ming Li, M. Konczykowski, and C. J. van der Beek

   Physica C 369, 36 (2002).

3. **Experimental upper bound on superradiance emission from Mn_{12}-acetate**

   M. Bal, J. R. Friedman, K. Mertes, W. Chen, E. M. Rumberger, D. N. Hendrickson, Nurit Avraham, Y. Myasoedov, H. Shtrikman, and E. Zeldov

   Phys. Rev. B 70, 140403(R) (2004).

4. **Photon-induced magnetization reversal in the Fe_8 single-molecule magnet**

M. Bal, J. R. Friedman, Yoko Suzuki, K. Mertes, E. M. Rumberger, D. N. Hendrickson, Y. Myasoedov, H. Shtrikman, Nurit Avraham, and E. Zeldov

Phys. Rev. B 70, 100408(R) (2004).

5. **The occurrence of avalanches in a single crystal of Mn_{12}-acetate**

   Yoko Suzuki, M. P. Sarachik, Nurit Avraham, Y. Myasoedov, H. Shtrikman, E. Zeldov, E. M. Rumberger, D. N. Hendrickson, and G. Christou

   J. Appl. Phys. 97, 10M517 (2005).

6. **Non-equilibrium magnetization dynamics in the Fe_8 single-molecule magnet induced by high-intensity microwave radiation**

   M. Bal, J. R. Friedman, Yoko Suzuki, E. M. Rumberger, D. N. Hendrickson, Nurit Avraham, Y. Myasoedov, H. Shtrikman, and E. Zeldov

   Europhys. Lett. 71, 110 (2005).

7. **Local Measurements of Magnetization in Mn_{12} Crystals**

   Nurit Avraham, Ady Stern, Yoko Suzuki, K. M. Mertes, M. P. Sarachik, E. Zeldov, Y. Myasoedov, H. Shtrikman, E. M. Rumberger, D. N. Hendrickson, N. E. Chakov, and G. Christou

   Phys. Rev. B 72, 144428 (2005).

8. **Propagation of Avalanches in Mn_{12}-Acetate: Magnetic Deflagration**

   Yoko Suzuki, M. P. Sarachik, E. M. Chudnovsky, S. McHugh, R. Gonzalez-Rubio, Nurit Avraham, Y. Myasoedov, E. Zeldov, H. Shtrikman, N. E. Chakov, and G. Christou

Phys. Rev. Lett. 95, 147201 (2005).

9. **Equilibrium first-order melting and second-order glass transitions of the vortex matter in** $Bi_2Sr_2CaCu_2O_8$

   H. Beidenkopf, Nurit Avraham, Y. Myasoedov, H. Shtrikman, E. Zeldov, B. Rosenstein, E. H. Brandt, and T. Tamegai

   Phys. Rev. Lett. 95, 257004 (2005).

10. **Photon-induced magnetization changes in single-molecule magnets**

    M. Bal, J. R. Friedman, E. M. Rumberger, S. Shah,D. N. Hendrickson, Nurit Avraham, Y. Myasoedov, H. Shtrikman and E. Zeldov

    J. Appl. Phys. 99, 08D103 (2006).

11. **Dynamic and thermodynamic properties of the porous vortex matter**

    Nurit Avraham, Y. Y. Goldschmidt, J. T. Liu, Y. Myasoedov, M. Rappaport, E. Zeldov, C. J. van der Beek, M. Konczykowski, and T. Tamegai

    Phys. Rev. Lett. 99, 087001 (2007).

10. BIBLIOGRAPHY

BIBLIOGRAPHY

[1] G. Bednorz and K.A. Müller, Z. Phys. B, **64**, 189 (1986).

[2] G. Blatter *et al.*, Rev. Mod. Phys. **66**, 1125 (1994).

[3] J. R. Friedman *et al.*, Phys. Rev. Lett **76**, 3830 (1996).

[4] W. Wernsdorfer *et al.*, Physica B **284**, 1231 (2000).

[5] H. Kamerlingh Onnes, Leiden Comm. 120b, 122b, 124c (1911).

[6] W. Meissner and R. Ochsenfeld, Naturwissenschaften **21**, 787 (1933).

[7] I. Giaever *et al.*, Phys. Rev. Lett. **5**, 147 (1960).

[8] F. London and H. London, Proc. Roy. Soc. (London) **A149**, 71 (1935).

[9] M. Tinkham, Introduction to Superconductivity, McGraw-Hill, Chapter 4 (1996).

[10] V. L. Ginzburg and L.D. Landau, Zh. Eksp. Teor. Fix, **20**, 1064 (1950).

[11] J. Bardeen, L. N. Cooper, and J. R. Schrieffer, Phys. Rev. **106**, 162 (1957).

[12] J. Bardeen, L. N. Cooper, and J. R. Schrieffer, Phys. Rev. **108**, 1175 (1957).

[13] L. N. Cooper, Phys. Rev. **104**, 1189 (1956).

[14] A.A. Abrikosov, Fundamental of the Theory of Metals, North Holland (1988).

[15] A.A Abrikosov, JETP, **5**, 1174 (1957).

[16] U. Essman and H. Traeuble, Phys. Lett. A **24**, 526 (1967).

[17] D. Criber, *et al.*, Phys. Status Solidi (b) **57**, 515 (1973).

[18] H. W. Weber, J. Scheller, and G. Lippman, Phys. Status Solidi (b), **57**, 515 (1973).

[19] J. Bosch *et al.* Phys. Rev. Lett. **54**, 1448 (1985).

[20] T. Matsuda, *et al.*, Phys. Rev. Lett. **62**, 2519 (1989).

[21] A. M. Change *et al.*, Europhys. Lett. **20**, 645, (1992).

[22] P.G. de Gennes, Superconductivity of Metals and Alloys, Addison-Wesley Publishing Co.,Chapter 6 (1966).

[23] B. Oh *et al.*, Phys. Rev. B **37**, 7861 (1988).

[24] D. R. Nelson, Phys. Rev. Lett. **60**, 1973 (1988).

[25] V. Vinokur *et al.*, Physica C **295**, 209 (1998).

[26] E. Brézin *et al.*, Phys. Rev. B **31**, 7124 (1985).

[27] H. Safar *et al.*, Phys. Rev. Lett. **69**, 824 (1992).

[28] D. T. Fuchs *et al.*, Phys. Rev. B **54**, R796 (1996).

[29] E. Zeldov *et al.*, Nature **375**, 373 (1995).

[30] H. Pastoriza *et al.*, Phys. Rev. Lett. **72**, 2951 (1994).

[31] R. A. Doyle *et al.*, Phys. Rev. Lett. **75**, 4520 (1995).

[32] A. Schilling *et al.*, Nature **382**, 451 (1996).

[33] R. Cubitt *et al.*, Nature **365**, 407 (1993).

[34] B. Khaykovich *et al.*, Phys. Rev. Lett. **76**, 2555 (1996).

[35] B. Khaykovich *et al.*, Phys. Rev. B **56**, R517 (1997).

[36] N. Avraham *et al.*, Nature **411**, 451 (2001).

[37] H. Beidenkopf, *et al.*, Phys. Rev. Lett. **95**, 257004 (2005).

[38] D. T. Fuchs *et al.*, Phys. Rev. Lett. **80**, 497 (1998).

[39] B. Khaykovich *et al.*, Physica C **282**, 2067 (1997).

[40] B. Khaykovich *et al.*, Phys. Rev. B **22**, R14088 (1998).

[41] L. M. Paulius *et al.*, Phys. Rev. B **61**, R11910 (2000).

[42] S. S. Banerjee *et al.*, Phys. Rev. Lett. **90**, 087004 (2003).

[43] S. S. Banerjee *et al.*, Phys. Rev. Lett. **93**, 097002 (2004).

[44] M. Menghini *et al.*, Phys. Rev. Lett. **90**, 147001 (2003).

[45] L. Radzihovsky, Phys. Rev. Lett. **74**, 4923 (1995).

[46] S. Tyagi and Y. Y. Goldschmidt, Phys. Rev. B. **67**, 214501 (2003).

[47] C. Dasgupta *et al.*, Phys. Rev. Lett. **91**, 127002 (2003).

[48] Y. Nonomura and X. Hu, Europhys. Lett. **65**, 533 (2004).

[49] A. V. Lopatin and V. M. Vinokur, Phys. Rev. Lett. **92**, 067008 (2004).

[50] Y. Y. Goldschmidt and E. Cuansing, Phys. Rev. Lett. **95**, 177004 (2005).

[51] L. Thomas. *et al.*, Nature **383**, 145 (1996).

[52] R. Sessoli, *et al.*, Nature **365**, 141 (1993).

[53] C. Sangregorio, *et al.*, Phys. Rev. Lett. **78**, 4645 (1997).

[54] B. Barbara, *et al.*, J. Magn. Magn. Mater. **140**, 1825 (1995).

[55] M. R. Pederson and S. N. Khanna Phys. Rev. B **60**, 9566 (1999).

[56] A. Soibel, Ph.D. Thesis, Weizmann Institute of Science, Rehovot, Israel (2001).

[57] A. Soibel *et al.*, Nature **406**, 282 (2000).

[58] M. Willemin *et al.*, Phys. Rev. B **58**, R5940 (1998).

[59] A. E. Koshelev, Phys. Rev. Lett. **83**, 178 (1999).

[60] G. P. Mikitik and E. H. Brandt, Supercond. Sci. Technol. **20**, S111 (2007).

[61] L. Klein *et al.*, Phys. Rev. B **48**, 3523 (1993).

[62] D. R. Nelson and V. M. Vinokur, Phys. Rev. B **48**, 13060 (1993).

[63] L. Civale *et al.*, Phys. Rev. Lett. **67**, 648 (1991).

[64] A. Silhanek *et al.*, Phys. Rev. B **59**, 13620 (1999).

[65] B. Hayani *et al.*, Phys. Rev. B **61**, 717 (2000).

[66] R. J. Drost *et al.*, Phys. Rev. B **58**, R615 (1998).

[67] N. Kameda *et al.*, Phys. Rev. B **72**, 064501 (2005).

[68] C. J. van der Beek *et al.*, Phys. Rev. Lett. **74**, 1214 (1995).

[69] W. S. Seow *et al.*, Phys. Rev. B **53**, 14611 (1996).

[70] V. Hardy *et al.*, Phys. Rev. B **54**, 656 (1996).

[71] Tilting **B** by $\pm 45^\circ$ requires tilting H_a by $\pm 40^\circ$ (found experimentally) since H_z is screened more efficiently by in-plane equilibrium shielding currents, compared to H_{ab}.

[72] B. Schmidt *et al.*, Phys. Rev. B **55**, R8705 (1997).

[73] S. Ooi *et al.*, Phys. Rev. Lett. **82**, 4308 (1999).

[74] H. Nordborg and G. Blatter, Phys. Rev. B **58**, 14556 (1998).

[75] S. Tyagi and Y. Y. Goldschmidt, Phys. Rev. B **70**, 024501 (2004).

[76] Y. Y. Goldschmidt, Phys. Rev. B **72**, 064518 (2005).

[77] Y. Y. Goldschmidt and S. Tyagi, Phys. Rev. B **71**, 014503 (2005).

[78] J. R. Clem, Phys. Rev. B **43**, 7837 (1991).

[79] L. N. Bulaevskii *et al.*, Phys. Rev. Lett. **77**, 936 (1996).

[80] Y. Y. Goldschmidt and J. T. Liu, Phys. Rev. B **76**, 174508 (2007).

[81] D. R. Nelson and V. M. Vinokur, Phys. Rev. Lett. **68**, 2398 (1992).

[82] M. V. Indenbom *et al.*, Phys. Rev. Lett. **84**, 1792 (2000).

[83] M. V. Indenbom *et al.*, Physica C **235**, 2001 (1994).

[84] E. Zeldov *et al.*, Phys. Rev. Lett. **73**, 1428 (1994).

[85] M. V. Indenbom and E. H. Brandt, Phys. Rev. Lett. **73**, 1731 (1994).

[86] C. P. Been and J.D. Livingston, Phys. Rev. Lett. **12**, 14 (1964).

[87] L. Burlachkov *et al.*, Phys. Rev. B **54**, 6750 (1996).

[88] M. Nideröst *et al.*, Phys. Rev. Lett. **12**, 3231 (1998).

[89] J. K. Gregory *et al.*, Phys. Rev. B **64**, 13451571 (2001).

[90] Y. M. Wang *et al.*, Phys. Rev. B **65**, 1345181 (2002).

[91] E. H. Brandt and G. P. Mikitik, Phys. Rev. Lett. **89**, 027002 (2002).

[92] G. P. Mikitik and E. H. Brandt, Phys. Rev. B **67**, 104511 (2003).

[93] G. P. Mikitik and E. H. Brandt, Phys. Rev. B **69**, 134521 (2004).

[94] A. Wahl *et al.*, Physica C **250**, 163 (1995).

[95] C. J. van der Beek *et al.*, Phys. Rev. B **54**, R792 (1996).

[96] R. J. Drost *et al.*, Phys. Rev. B **58**, R615 (1998).

[97] C. J. van der Beek *et al.*, Phys. Rev. B **61**, 4259 (2000).

[98] G. S. Mkrtchyan, V.V. Shmidt, Sov. Phys. JETP **34**, 195 (1971).

[99] A. I. Buzdin, Phys. Rev. B **47**, 11416 (1993).

[100] R. A. lehrer and D. R. Nelson, Physica C **331**, 317336 (2000).

[101] D. R. Nelson and V. M. Vinokur, Phys. Rev. Lett. **68**, 2398 (1992).

[102] C. J. van der Beek *et al.*, Phys. Rev. B **51**, 15492 (1995).

[103] A. Soibel *et al.*, Nature **406**, 282 (2000).

[104] See http://www.weizmann.ac.il/home/fnsup/movies/72K.avi for a movie of the transition from Meissner to mixed state at 72 K in the presence of shaking.

[105] R. J. Drost *et al.*, Phys. Rev. B **59**,13612 (1999).

[106] E. H. Brandt Phys. Rev. B **68**, 054506 (2003).

[107] A. I. Larkin and V. M. Vinokur, Phys. Rev. Lett. **75**, 4666 (1995).

[108] A. Caneschi *et al.*, J. Am. Chem. Soc. **113**, 5873 (1991).

[109] R. Sessoli *et al.*, J. Am. Chem. Soc **115**, 1804 (1993).

[110] R. Sessoli, Mol. Cryst. Liq. Cryst. **274**, A 145 (1995).

[111] M. A. Novak *et al.*, J. Magn. Magn. Mater. **146**, 211 (1995).

[112] C. Paulsen and J.-G. Park, in Quantum Tunneling of Magnetization, edited by L. Guther and B. Barbara (Kluwer, Amsterdam/Dordrecht, 1995) (p. 189).

[113] M. A. Novak and R. Sessoli, in Quantum Tunneling of Magnetization, edited by L. Guther and B. Barbara (Kluwer, Amsterdam/Dordrecht, 1995) (p. 171).

[114] C. Paulsen *et al.*, J. Magn. Magn. Mater. **140-144**, 1891 (1995).

[115] T. Lis, Acta Crystallogr. Sec. B **36**, 2042 (1980).

[116] C. Paulsen *et al.*, J. Magn. Magn. Mater. **140-144**, 379 (1995).

[117] A. L. Barra *et al.*, Phys. Rev. B **56**, 8192 (1997).

[118] S. Hill *et al.*, Phys. Rev. Lett. **80**, 2453 (1998).

[119] I. Mirebeau *et al.*, Phys. Rev. Lett. **83**, 628 (1999).

[120] J. R. Friedman *et al.*, Jour. Appl. Phys. **79**, 6031 (1996).

[121] J. M. Hernandez *et al.*, Phys. Rev. B **55**, 5858 (1997).

[122] J. D. Jackson, Classical Electrodynamics, John Wiley and Sons, third edition (Eq. 5.56).

[123] W. Wernsdorfer *et al.*, Phys. Rev. Lett **82**, 3903 (1999).